

N O T I C E

THIS DOCUMENT HAS BEEN REPRODUCED FROM
MICROFICHE. ALTHOUGH IT IS RECOGNIZED THAT
CERTAIN PORTIONS ARE ILLEGIBLE, IT IS BEING RELEASED
IN THE INTEREST OF MAKING AVAILABLE AS MUCH
INFORMATION AS POSSIBLE

Application of Digital Image Processing Techniques to Astronomical Imagery 1979

Jean J. Lorre

(NASA-CR-162877) APPLICATION OF DIGITAL
IMAGE PROCESSING TECHNIQUES TO ASTRONOMICAL
IMAGERY, 1979 (Jet Propulsion Lab.) 75 p
HC A04/MF A01

N80-19996

CSCL 03A

G3/89

Unclas
47585

November 1, 1979



National Aeronautics and
Space Administration

Jet Propulsion Laboratory
California Institute of Technology
Pasadena, California

JPL PUBLICATION 79-109

Application of Digital Image Processing Techniques to Astronomical Imagery 1979

Jean J. Lorre

**ORIGINAL CONTAINS
COLOR ILLUSTRATIONS**

November 1, 1979

National Aeronautics and
Space Administration

Jet Propulsion Laboratory
California Institute of Technology
Pasadena, California

PREFACE

The work described in this report was performed by the Observational Systems Division of the Jet Propulsion Laboratory.

ACKNOWLEDGMENTS

The activities described in this report were encouraged by Dr. Nancy Roman, Dr. Jeffrey Rosendahl, and Dr. Edward Weiler at NASA Headquarters. William B. Green, Manager of the Science Data Analysis Section which includes the JPL Image Processing Laboratory, was instrumental in supporting this project. I wish to thank Dr. Stephen Gull of Cavendish Laboratories for his algorithm implementing the Maximum Entropy concept; Drs. Halton Arp and Jack Sulentic of Hale Observatories for their suggestions and plates of M87; Dr. Allan Sandage of Hale Observatories for his suggestions and plates of M82; and Peter Kupferman of JPL for his relentless efforts to reduce the silicon vidicon images of planetary nebulae and to master VICAR.

PRECEDING PAGE BLANK NOT FILMED

ABSTRACT

Several areas of applications of image processing to astronomy have been identified and developed in this report. These areas include:

1. Deconvolution for atmospheric seeing compensation; a comparison between maximum entropy and conventional Wiener algorithms.
2. Polarization in galaxies from photographic plates.
3. Time changes in M87 and methods of displaying these changes.
4. Comparing emission line images in planetary nebulae.
5. Log Intensity, Hue Saturation Intensity, and Principal Component color enhancements of M82.
6. Decalibration of CCD arrays for spatial sensitivity variations.

Examples are presented of these techniques applied to a variety of objects.

CONTENTS

I. INTRODUCTION	1-1
II. DECONVOLUTION - MAXIMUM ENTROPY VS. WIENER	2-1
III. POLARIZATION IN GALAXIES	3-1
IV. TIME CHANGES IN M87	4-1
V. PLANETARY NEBULAE - COMPARING EMISSION LINE IMAGES	5-1
VI. COLOR ENHANCEMENTS	6-1
A. LOG INTENSITY STRETCH	6-1
B. HSI	6-3
C. PRINCIPAL COMPONENT	6-5
VII. DECALIBRATION OF CCD ARRAYS	7-1
VIII. SUMMARY AND CONCLUSIONS	8-1
REFERENCES	9-1

Figures

1. Maximum entropy vs. Wiener restoration on a noiseless blurred target	2-3
2. Maximum entropy vs. Wiener restoration on a blurred target with an RMS = 30 noise level added	2-4
3. Maximum entropy vs. Wiener restoration on a blurred target with an RMS = 60 noise level added	2-5
4. Maximum entropy vs. Wiener restoration on a blurred noiseless target	2-6
5. Maximum entropy vs. Wiener restoration on a real scene of M87. Bottom row are each Wiener restorations with signal-to-noise ratios of 4, 8, and 14	2-7
6. Maximum entropy vs. Wiener restoration on a real scene of M87	2-8
7. Maximum entropy restoration of blurred decimated images	2-9

8.	Maximum entropy vs. Wiener restorations for one-dimensional spectra -----	2-10
9.	Maximum entropy vs. Wiener restoration for an RMS noise of 2 added to the degraded image -----	2-11
10.	Maximum entropy vs. Wiener restoration for an RMS noise of 6 added to the degraded image -----	2-12
11.	M82 difference image in the sense \vec{E} -vector along the major axis minus \vec{E} -vector normal to the major axis -----	3-3
12.	M82 polarization image scaled with 25 percent polarization to white -----	3-4
13.	M82 polarization image in the same format as Figure 12, but computed from smoothed images -----	3-5
14.	M87 mosaic displaying four polarization orientations, each in 6- and 3-minute exposures and each at two epochs, 1956 and 1978 -----	4-2
15.	M87 difference images in the sense 1978 minus 1956, each in four polarization orientations -----	4-3
16.	M87 difference images in the same format as Figure 15 -----	4-4
17.	NGC6720 mosaic of nine emission line images after radiometric correction and scaling for visual interpretation -----	5-4
18.	NGC6720 two-dimensional Fourier transforms displayed as log amplitude in a one-to-one correspondence with the images of Figure 17 -----	5-5
19.	NGC6720 mosaic of modified transforms in the same format as Figure 18 -----	5-6
20.	NGC6720 mosaic in the same format as Figure 17 after the reduction of all noise sources -----	5-7
21.	NGC6720 mosaic of polar coordinate transformations in the same order as Figure 20 -----	5-8
22.	NGC6720 mosaic of the volume emission coefficient at different wavelengths suitably scaled for viewing -----	5-9
23.	NGC6720 temperature map scaled for viewing -----	5-10
24.	NGC6720 electron density map scaled for viewing -----	5-11
25.	NGC6720 mosaic of different images color coded green and added to the H α image coded red -----	5-12

26. NGC6720 color-coded rendition of ionization structure.
Color assignments are blue = HeII, 4686; green = HeI, 5876;
red = [OI], 6300 ----- 5-13
27. NGC6720 color-coded rendition of ionization structure. Color
assignments are blue = [OII], 3727; green = [OIII], 5007;
red = [OI], 6300 ----- 5-14
28. M82 mosaic of four combinations of three colors each ----- 6-8
29. M82 mosaic after the Log Intensity transformation which
preserves but does not enhance color differences ----- 6-9
30. M82 mosaic after Log Intensity transformation but coded
with log intensity in equal reflectance steps ----- 6-10
31. M82 mosaic of the four individual colors after the Log
Intensity transformation ----- 6-11
32. M82 mosaic of three structural bands ----- 6-12
33. M82 mosaic in the same format as Figure 32. From the top
down, the left column pictures are 103a0, 103aD, and Ha ----- 6-13
34. M82 mosaic in the same format as Figure 32. From the top
down, the left column pictures are 103a0, 103aE, and Ha ----- 6-14
35. M82 mosaic in the same format as Figure 32. From the top
down, the left column pictures are 103aD, 103aE, and Ha ----- 6-15
36. M82 mosaic after HSI color enhancement with the hue,
saturation, and intensity transformation and coded with
log intensity in equal density steps ----- 6-16
37. M82 mosaic after HSI color enhancement the same as
Figure 36, except with log intensity coded into equal
reflectance steps ----- 6-17
38. M82 mosaic of pure hue after discarding the saturation
and intensity images in the HSI transformation ----- 6-18
39. M82 mosaic of the principal component images produced
from four spectral bands ----- 6-19
40. M82 mosaic of color-enhanced reconstructions from the
principal component images of Figure 39 ----- 6-20
41. M82 mosaic of color-enhanced images produced the same
way as Figure 40, but with an intermediate filter which
smoothed in inverse proportion to the information content
of each principal component band ----- 6-21
42. Scaled display of the response of a CCD array to a flat
field stimulus ----- 7-3

43.	Scaled display of the multiplicative term of the calibration file used to decalibrate the CCD image of Figure 42 -----	7-4
44.	Scaled display of the offset term of the calibration file used to decalibrate the CCD image of Figure 42 -----	7-5
45.	Scaled decalibrated CCD flat field image -----	7-6
46.	Variance image displaying the variances of each pixel in a set of five identical exposures in an undecalibrated field -----	7-7

Tables

1.	Wavelengths of Each Planetary Nebula Image -----	5-1
2.	Color Assignments of Narrow Band Images for Figures 26 and 27 -----	5-3
3.	Standard Color Assignments for the M82 Mosaics -----	6-2
4.	Emulsion/Filter Combinations -----	6-2
5.	Assignments of Bands to Primaries in Figures 32 through 35 --	6-4
6.	Information Content in Each Principal Component Image of M82 for Figure 39 -----	6-6

SECTION I

INTRODUCTION

Astronomy has traditionally made great use of imagery, but this data has almost exclusively been evaluated via the photographic process. With the advent of the unmanned planetary missions and digital cameras, techniques for processing digital images have been developed and are beginning to be applied in astronomy. The advantages of digital images over photographic ones are very great and, with the development of new algorithms and cameras, become greater all the time. It is thus of importance to search for applications and disseminate digital techniques to the astronomical community at large. When Space Telescope becomes operational, the quantity and unprecedented quality of the calibrated digital images returned will call for every available processing means at our disposal. This report is intended to provide a few of those means.

This work was performed during 1979 at the Image Processing Laboratory (IPL) of JPL under FY79 RTOP #389-41-01. It represents a continuing effort (References 1 and 2) to identify and develop new image processing applications to astronomy. Additional goals of this research are the further education of the astronomical community in digital image processing techniques and the expansion of methods for analysis of high-quality space telescope imagery when it becomes available. Hopefully, others will be inspired to find applications to their own disciplines.

This report is divided into eight sections. Sections II through VII present techniques applied to a major topic. The data used and the techniques involved are described in detail, along with photographs and plots of the results. Section VIII gives conclusions that can be made as a result of this work. This report illustrates image processing and does not interpret the physical significance of results that develop from the data. The role of data interpretation resides with the collaborating astronomer. Image processing is a vehicle to strengthen and simplify his task.

SECTION II

DECONVOLUTION - MAXIMUM ENTROPY VS. WIENER

The algorithm developed by Dr. Gull and Dr. Daniell (References 3 and 4) for correcting incomplete radio maps was provided in a form suitable for deconvolution of optical images (Reference 5). This technique has proven very successful in restoring Fourier transforms, and the philosophy is applicable to solving, in an iterative fashion, the general inverse problem.

The maximum entropy technique has several desirable properties which are not observed by linear filters:

- (1) It produces a unique map.
- (2) The restored intensity values are non-negative.
- (3) Ringing (Gibbs phenomena) is virtually undetectable.

To provide a control, an 8-bit synthetic image was created (upper left corner of Figure 1). This image was convolved with a 5-by-5 element kernel of equal weight which replaced each pixel by the means of its neighborhood (upper right of Figure 1). The object was to restore the degraded image to its original form. In the central row of Figure 1, the left image represents the maximum entropy restoration and the right image represents the Wiener linear restoration (References 6 and 7). The lower left image of Figure 1 contains the chi squared residuals map of the maximum entropy restoration, i.e., the ratio of misfit to the data to the error due to noise in the data. The lower right image of Figure 1 contains the log MTF of the kernel used to degrade the original, i.e., the log modulus of the Fourier transform of the 5-by-5 element point spread function. This particular kernel is not trivial to correct for because it introduces both 180° phase shifts and crosses the zero amplitude plane (dark bars) in many places.

In the case illustrated by Figure 1 (which is noiseless if one can disregard the RMS integer truncation noise of $1/2\sqrt{3}$), the Wiener model, even with a modest signal-to-noise ratio of 15, is more effective for visual recognition.

Figures 2 and 3 demonstrate the effect of adding random noise to the degraded image before restoration in RMS quantities of 30 and 60, respectively. In Figure 3, the true signal-to-noise ratio in the image is approximately unity and the linear model has been forced to further blur the data in order to improve it. The two algorithms operate with equal effectiveness in Figure 2. In Figure 3, the noise level is almost too high for either algorithm to effect an improvement.

In Figure 4, a larger filter of 9-by-9 elements has been employed, which has destroyed the control beyond the human pattern recognition capability to recognize any characters. No noise was added and the linear model was able to restore most of the image into the recognizable range.

It appears from the above exercise that the maximum entropy restoration is able to compensate for small amounts of blurring in the presence of noise and to produce relatively artifact-free images when the noise level is moderate. The Wiener model is superior from a subjective standpoint only in the low-noise regime.

To compare both algorithms on astronomical images, four plates taken through a polaroid at P.A. 245° of M87 were averaged. Reference stars were selected from the field and placed into a row at the bottom of the image. These stars provided the required point spread function. Figure 5 illustrates a mosaic of several images of M87. On the top row the left image is the original, the middle is the maximum entropy restored version, and the right image is the chi squared residuals map. On the bottom row from left to right are linear Wiener model restorations with signal-to-noise values of 4, 8, and 14. The maximum entropy restoration is virtually artifact free but is only slightly enhanced. The Wiener restorations, although full of artifacts, provide better restoration where the signal-to-noise ratio is high. The background artifact is due to the linear model's assumption that the signal-to-noise ratio is independent of position. It is ironic that the chi squared residuals map is as interesting as the restoration. In Figure 6, a similar picture to Figure 5 is presented, which provides a better maximum entropy restoration. This was accomplished by smoothing the original image with a small convolutional filter, thus improving the overall signal-to-noise ratio by suppressing the highest frequencies.

It is important to consider that, because the maximum entropy technique produces little artifact, it may be more valuable to employ in cases where the true nature of the object cannot be estimated beforehand.

One of the powerful capabilities of the maximum entropy restoration is its ability to assign noise weighting to the image on a pixel-to-pixel basis. As an example of this, the control image used in Figure 1 was degraded with a 7-by-7 kernel and then decimated with a random grid (shown at the bottom left of Figure 7). The lower right of Figure 7 shows the restoration. Although this restoration is not better than the blurred version, the application of any linear convolutional model would have resulted in a totally unrecognizable picture.

A comparison of both algorithms was also performed upon synthetic spectra in order to evaluate their performance in one dimension. Each of the three figures, Figures 8, 9, and 10, contains the original spectrum at the top, the degraded and noise added spectrum at the bottom and, in the second and third rows from the top, the maximum entropy and Wiener model restorations respectively. The object was, as usual, to reconstruct the top row from the bottom one. Figures 8, 9, and 10 differ insofar as the RMS noise added to the degraded spectrum was zero for Figure 8; two for Figure 9; and six for Figure 10; with corresponding Wiener signal-to-noise values of 20, 10, and 4. From a comparison of Figures 8, 9, and 10, it can be seen that once again as in the case of the two-dimensional restorations the linear model is superior when the noise level is very low. At intermediate noise levels, the two algorithms are very similar, and, at high noise levels, they become equally unreliable, producing artifacts.



ORIGINAL PAGE IS
 OF POOR QUALITY

Figure 1. Maximum entropy vs. Wiener restoration on a noiseless blurred target: (top left) original; (top right) blurred target; (center left) maximum entropy restoration; (center right) Wiener restoration; (lower left) maximum entropy chi squared residuals; (lower right) transfer function of the degrading filter, a 5-by-5 element box filter. The Wiener signal-to-noise ratio was 15.

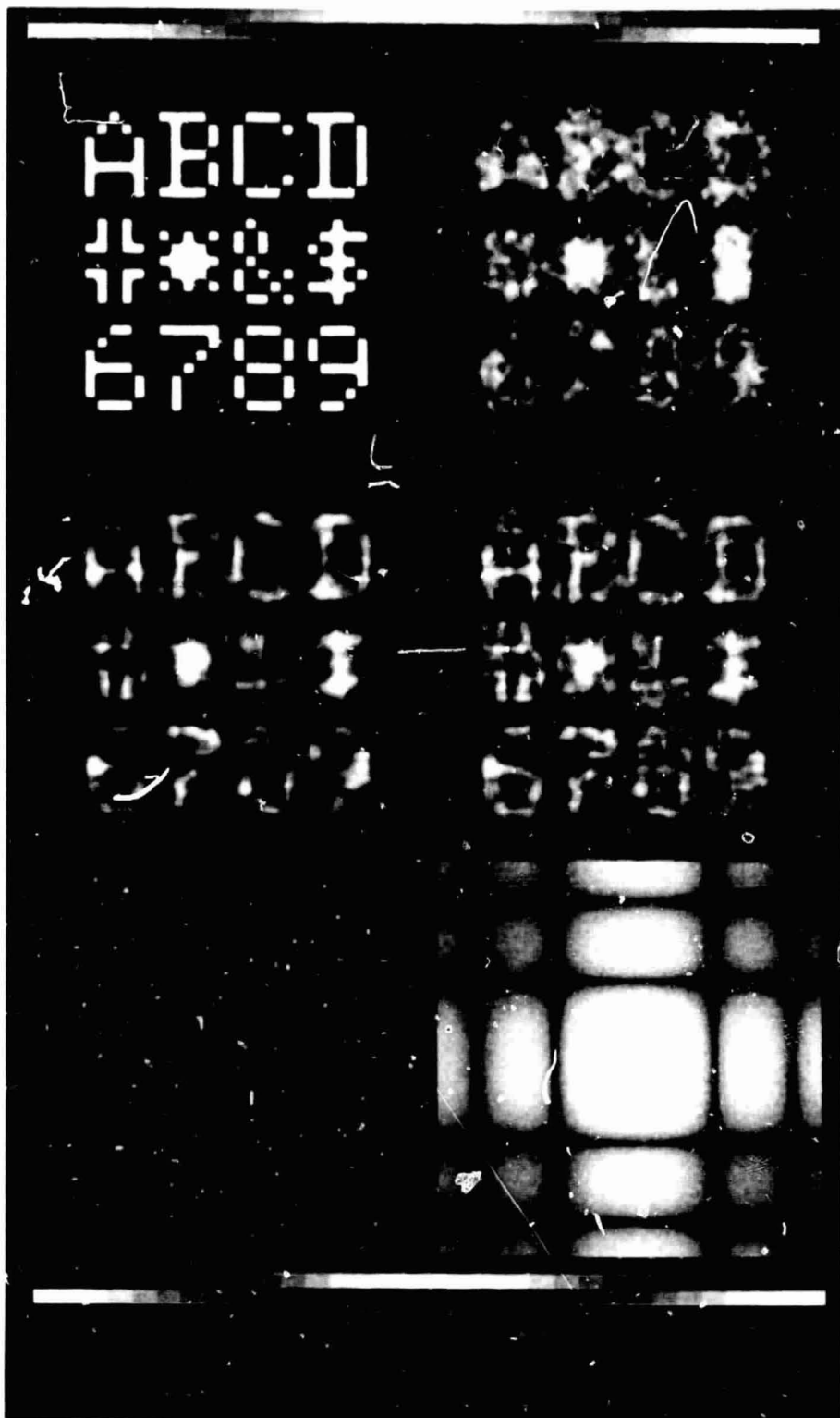


Figure 2. Maximum entropy vs. Wiener restoration on a blurred target with an RMS = 30 noise level added. The wiener signal-to-noise ratio was 5.



ORIGINAL PAGE IS
OF POOR QUALITY

Figure 3. Maximum entropy vs. Wiener restoration on a blurred target with an RMS = 60 noise level added. The Wiener signal-to-noise ratio was 2.5.



Figure 4. Maximum entropy vs. Wiener restoration on a blurred noiseless target. The degrading filter was increased in size to 9-by-9 elements.

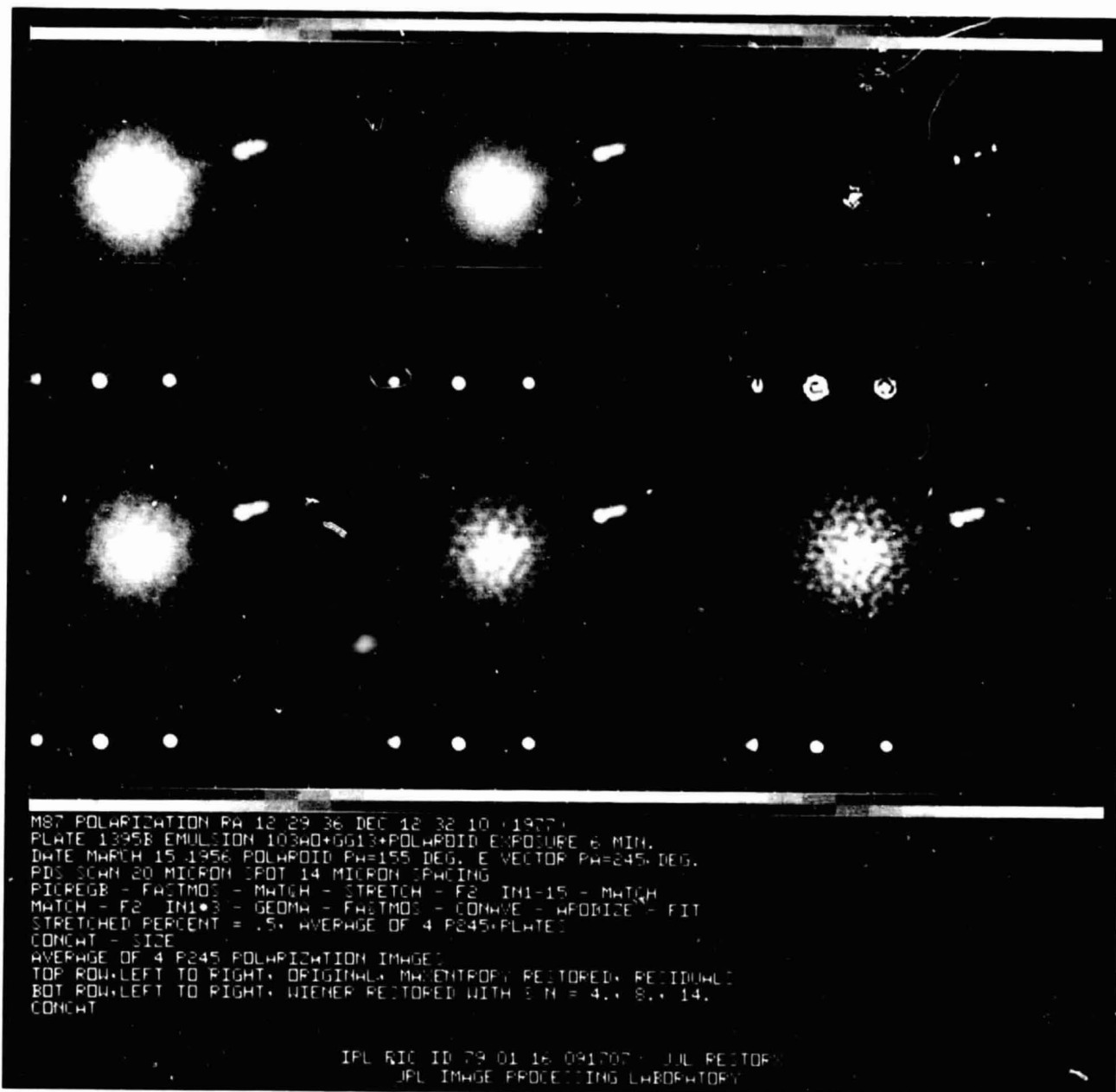


Figure 5. Maximum entropy vs. Wiener restoration on a real scene of M87: (top left) original; (top middle) maximum entropy restoration; (top right) chi squared residuals. Bottom row are each Wiener restorations with signal-to-noise ratios from left to right of 4, 8, and 14.

ORIGINAL PAGE IS
 OF BEST QUALITY



Figure 6. Maximum entropy vs. Wiener restoration on a real scene of M87: (top left) smoothed original; (middle) maximum entropy restoration; (right) chi squared residuals.

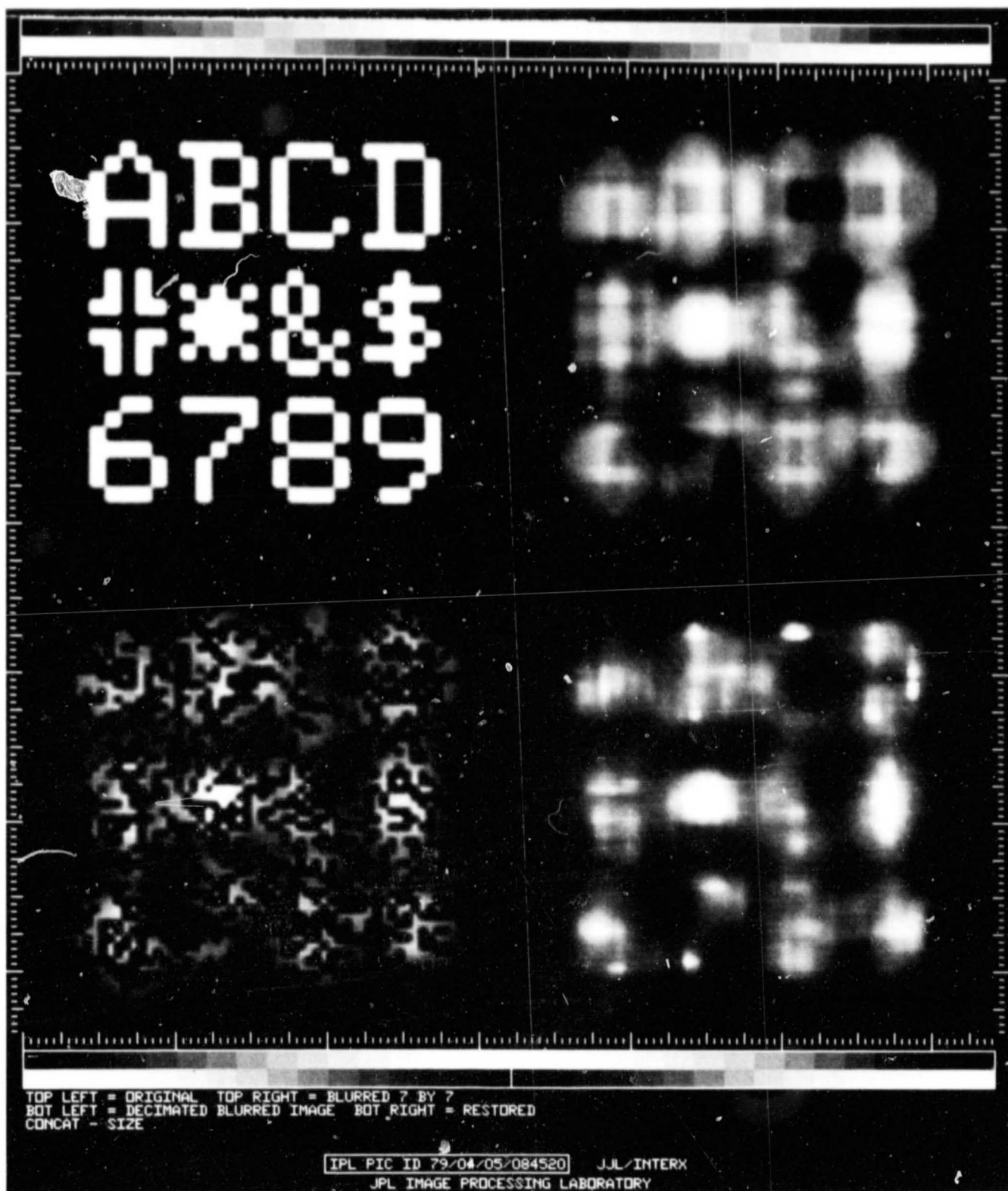


Figure 7. Maximum entropy restoration of blurred decimated images: (top left) original; (top right) blurred image; (lower left) decimated image; (lower right) restoration.

ORIGINAL PAGE IS
OF POOR QUALITY

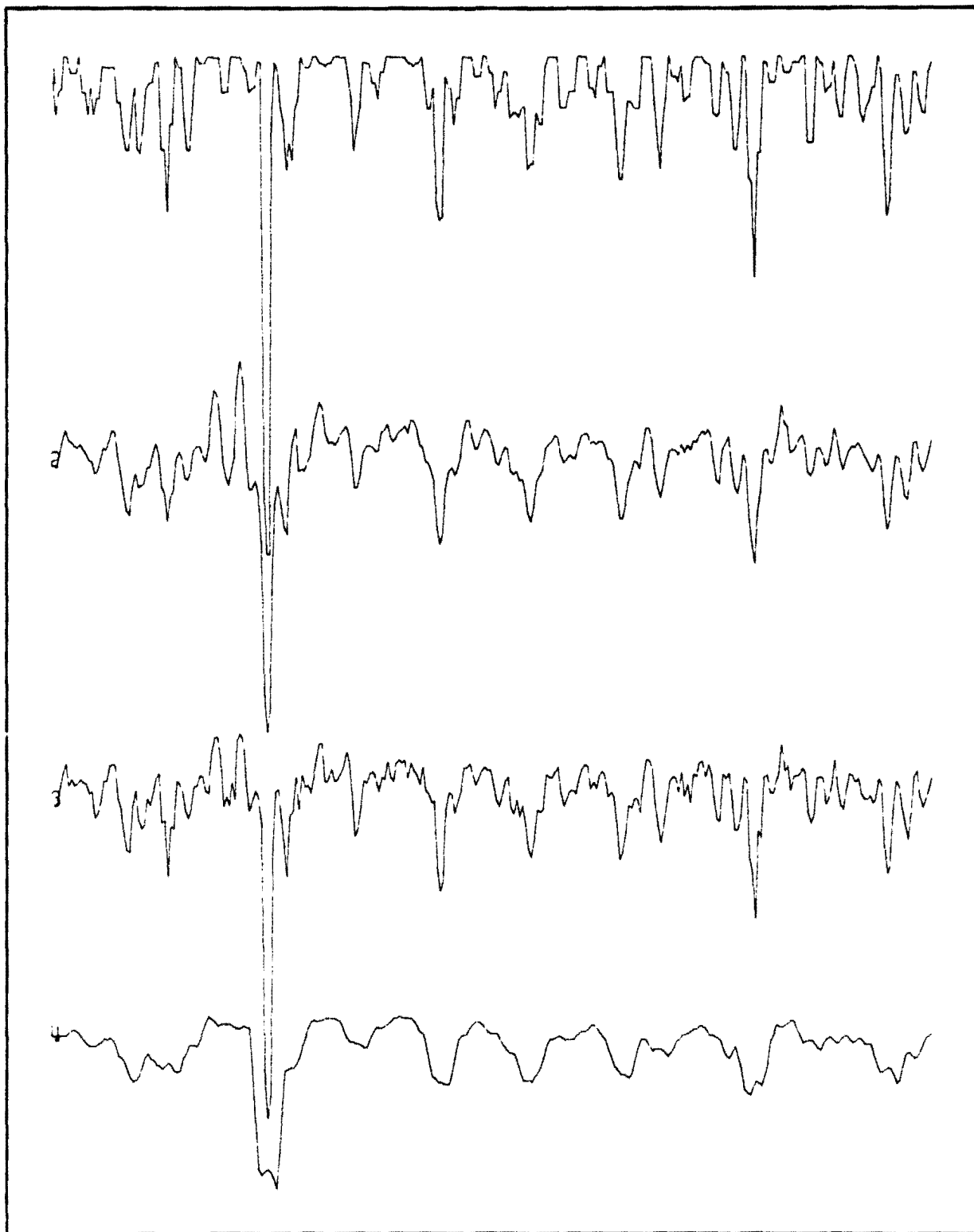


Figure 8. Maximum entropy vs. Wiener restorations for one-dimensional spectra: (top) original spectrum; (bottom) noiseless degraded spectrum; (second row) maximum entropy restoration; (third row) Wiener restoration with a signal-to-noise ratio of 20.

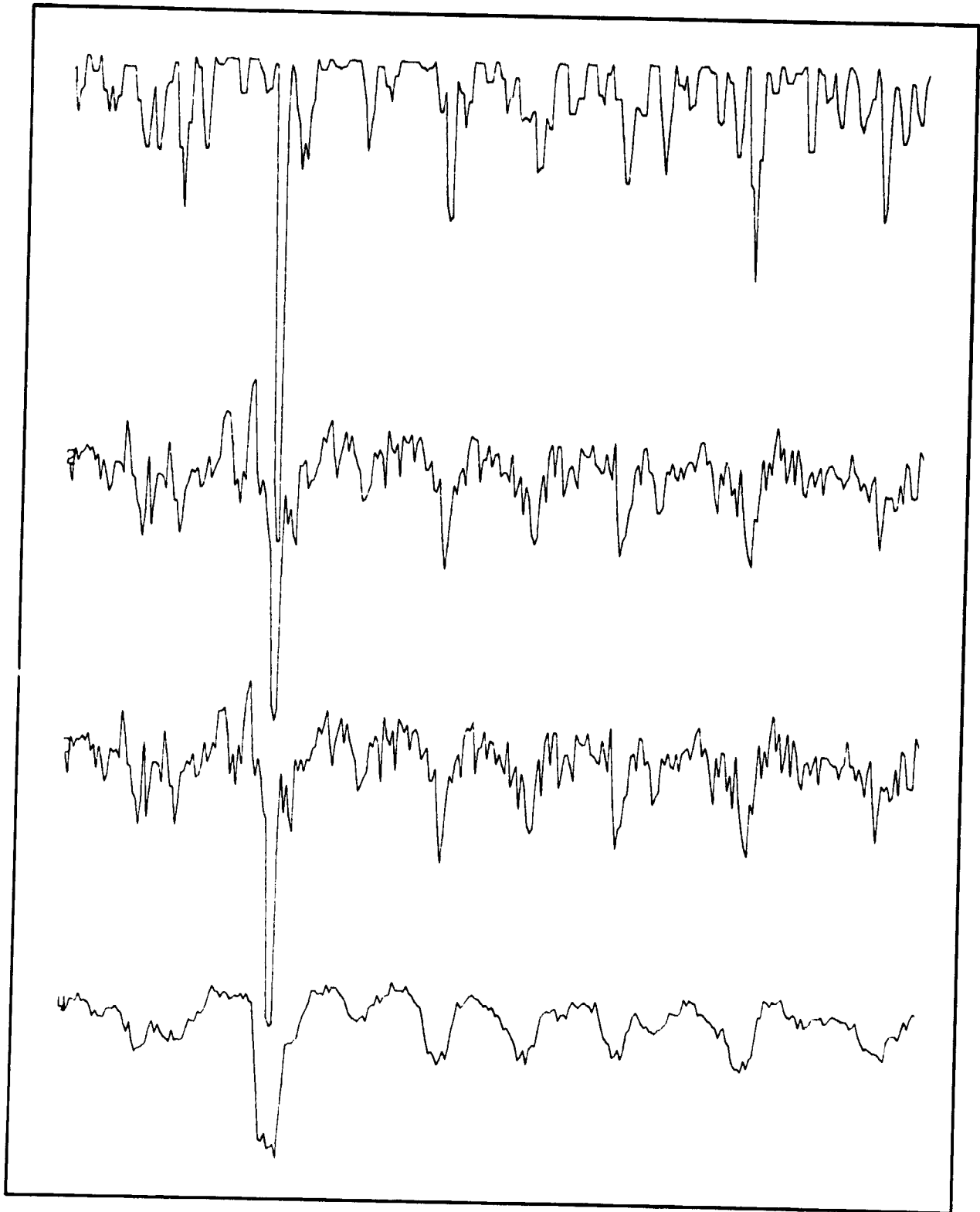


Figure 9. Maximum entropy vs. Wiener restoration for an RMS noise of 2 added to the degraded image. The Wiener signal-to-noise ratio used was 10.

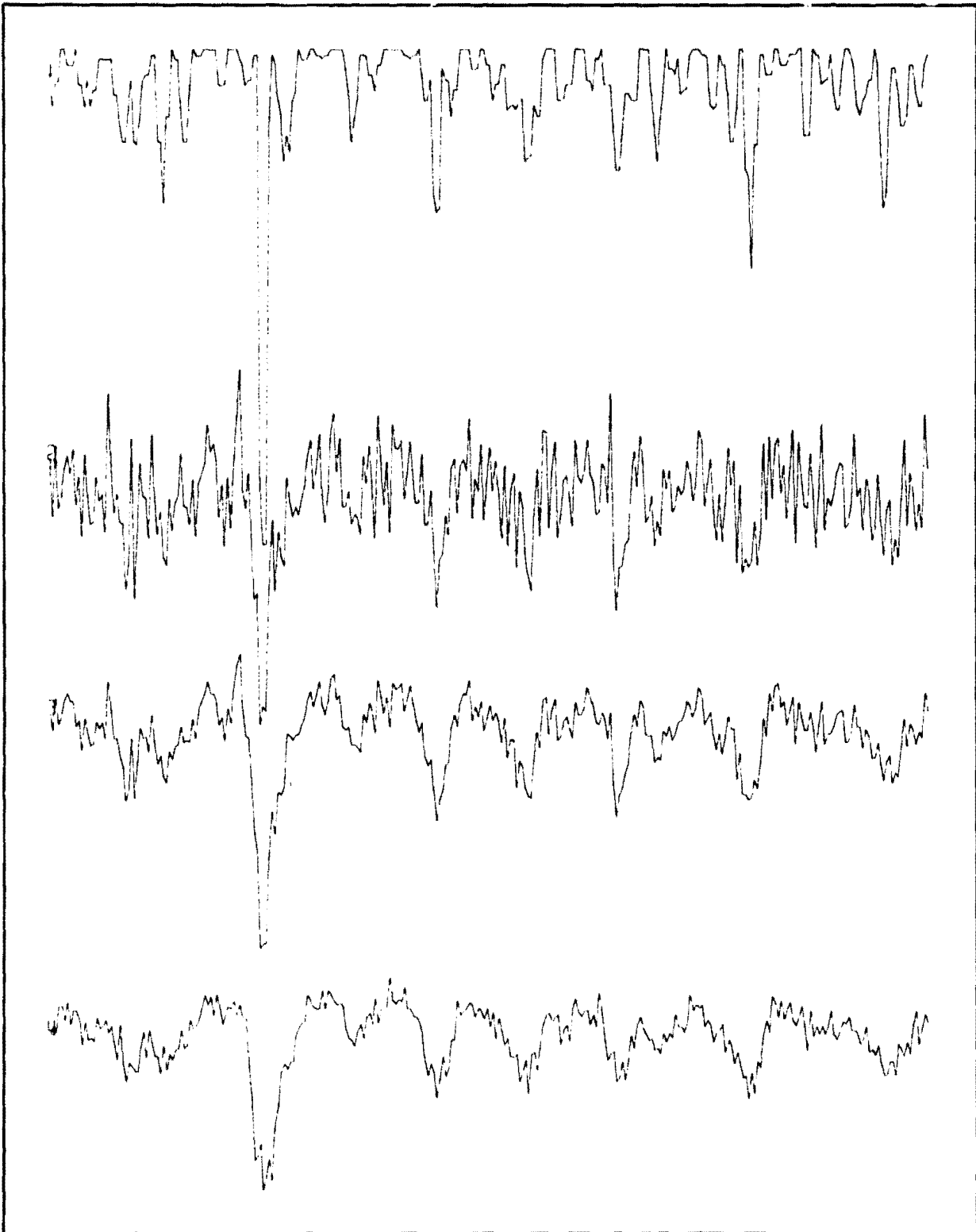


Figure 10. Maximum entropy vs. Wiener restoration for an RMS noise of 6 added to the degraded image. The Wiener signal-to-noise ratio used was 4.

SECTION III

POLARIZATION IN GALAXIES

Plates of M82 obtained by Dr. Allan Sandage of Hale Observatories in two polarization orientations were scaled such that the mean sky level was centered at zero and the variances of both images were identical. Even though only two \vec{E} -vector orientations were known, it was possible to compute the polarization because the direction of the polarization vector was known to be approximately tangential about the center of the M82 nucleus (Reference 8).

Figure 11 illustrates the difference between two images in the sense \vec{E} -vector along major axis minus \vec{E} -vector along minor axis. Much filamentary structure is visible, all due to polarization. For the case of four \vec{E} -vector positions 45° apart, the polarization can be computed from Equations 1 through 4.

$$\frac{Q}{I} = \frac{I_{0^\circ} - I_{90^\circ}}{I_{0^\circ} + I_{90^\circ}} \quad (1)$$

$$\frac{U}{I} = \frac{I_{45^\circ} - I_{135^\circ}}{I_{45^\circ} + I_{135^\circ}} \quad (2)$$

$$\tan 2\theta = \frac{U}{Q} \quad (3)$$

$$P = \sqrt{\left(\frac{Q}{I}\right)^2 + \left(\frac{U}{I}\right)^2} \quad (4)$$

Relations (Eq. 1-3) can be combined to give

$$\frac{Q}{I} \tan 2\theta = \frac{U}{I} \quad (5)$$

and from this and relation (Eq. 4)

$$P = \frac{Q}{I} \sqrt{1 + \tan^2 2\theta} \quad (6)$$

the form when the angle is known. The $\tan^2 2\theta$ acts as a modulating term which corrects for the polarization amplitude at other than 0 and 90 degrees. At multiples of 90° beginning at 45° , the function becomes unstable and results in noise amplification, leaving a cross in the polarization picture. Figures 12 and 13 illustrate the polarization map of M82 both before and after local smoothing of the original images. In both cases 25 percent polarization is equivalent to white, and zero is equivalent to black. Because of the low signal-to-noise ratio near the plate background, low-intensity values become corrupted by noise and result in spuriously high polarization values giving rise to the white ring around M82. A threshold was applied to the algorithm which set the polarization to zero if the intensity in either frame fell below a certain level. This gave rise to the dark region outside the bright noise-induced halo. Due to assumptions made in scaling the images, the polarization on the bar of the galaxy is constrained to be zero. The filaments, which extend normal to the bar, are highly polarized at about 20 percent.

From inspection of the previous formula, it is clear that noise will severely influence the measure of polarization if either:

- (1) The differences between intensities are on the same order as the RMS noise.
- (2) The intensities are so low that their sums are on the same order as the RMS noise.

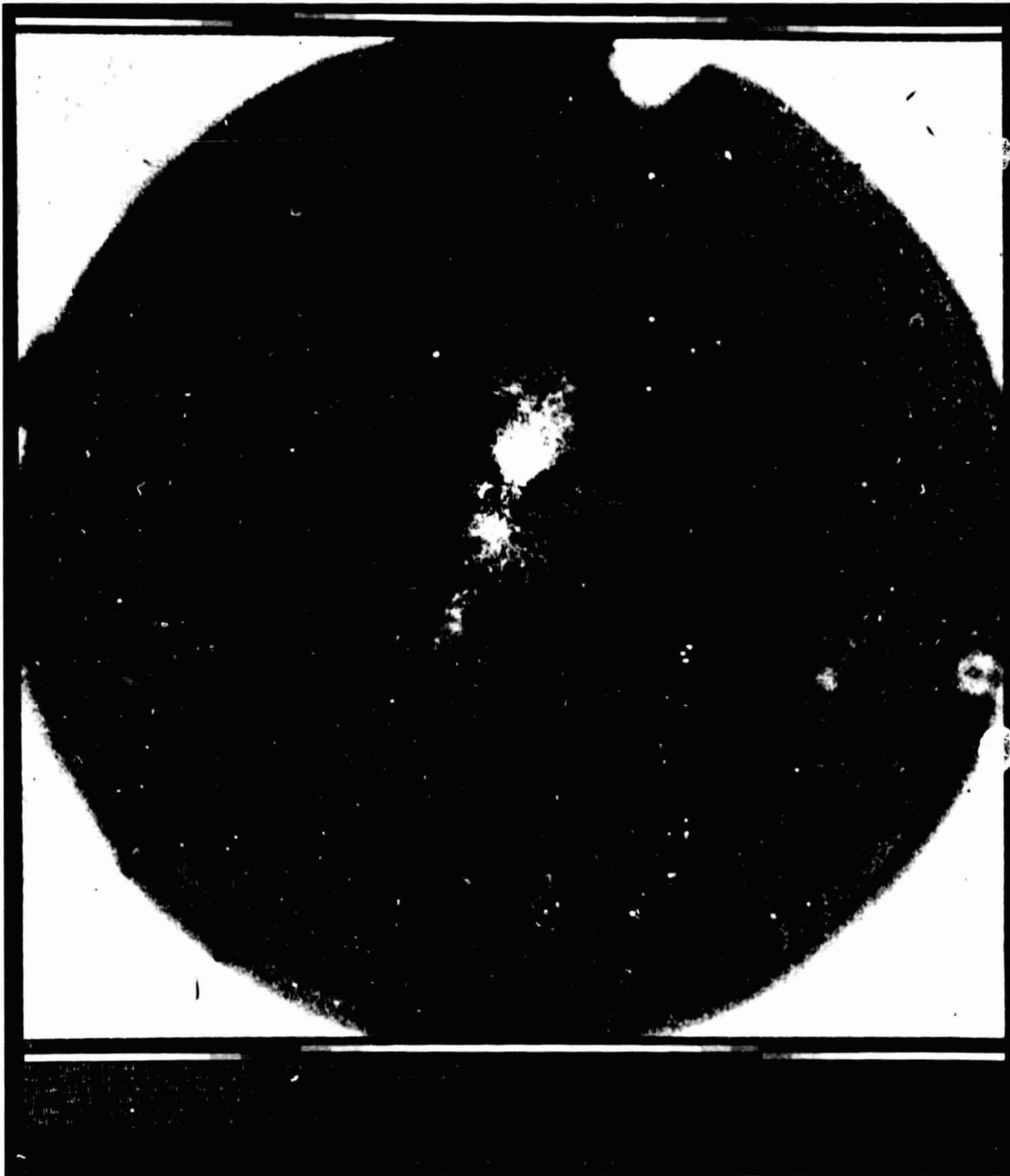


Figure 11. M82 difference image in the sense \vec{E} -vector along the major axis minus \vec{E} -vector normal to the major axis

ORIGINAL SIZE
OF FILE 1000000



Figure 12. M82 polarization image scaled with 25 percent polarization to white. The cross is artifact due to the assumed circumferential direction of the polarization vector. The white halo around M82 is artifact due to low signal-to-noise ratio close to the sky. Polarized filaments are visible in two quadrants above and below the cross center.

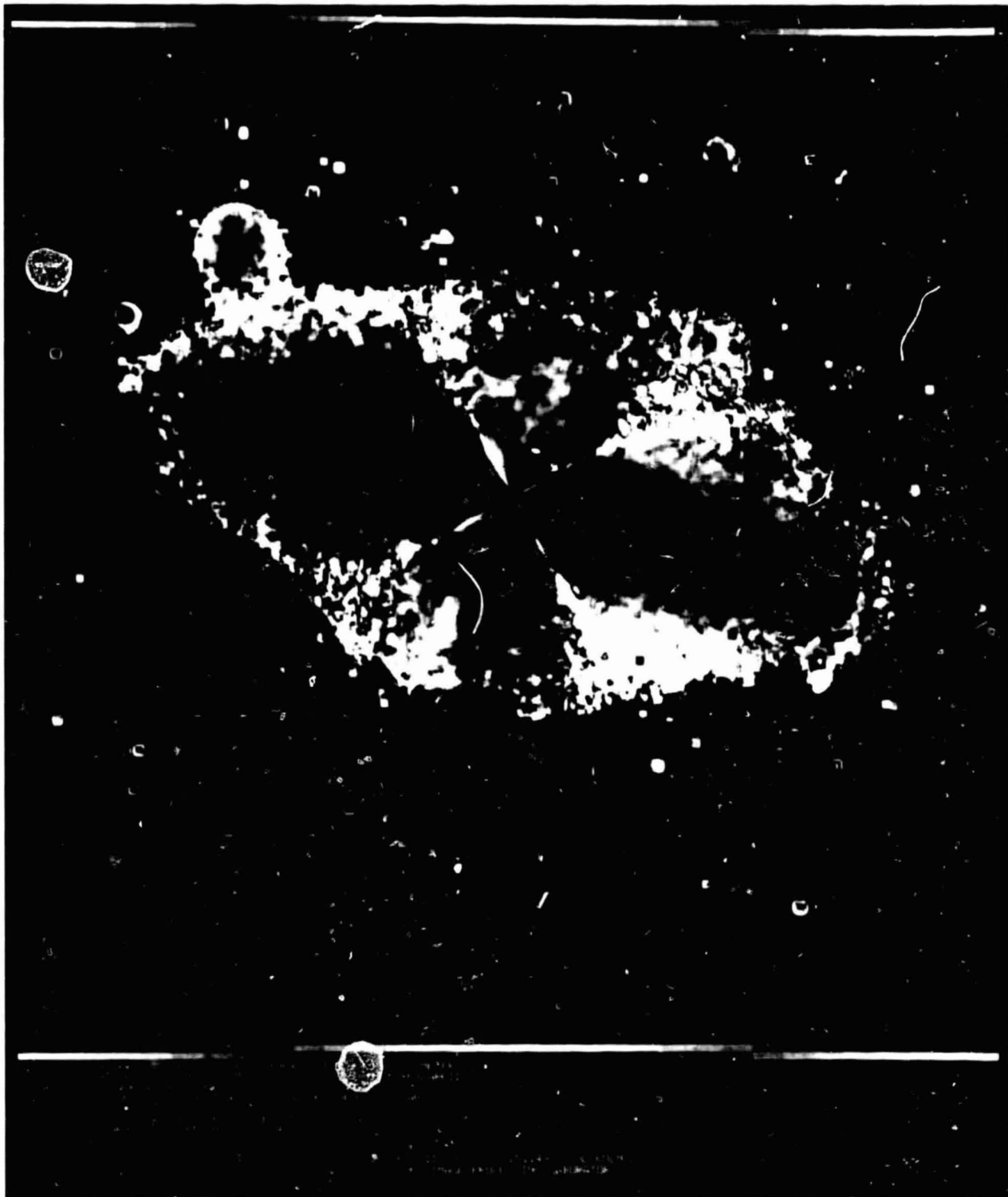


Figure 13. M82 polarization image in the same format as Figure 12,
but computed from smoothed images

SECTION IV

TIME CHANGES IN M87

Plates of M87 were taken in two epochs, one in 1956 by Dr. Baade and the other in 1978 by Drs. Arp and Sulentic of Hale Observatories. Each set of plates was recorded at 3- and 6-minute exposures and each at four polarization orientations. A mosaic of all sixteen images is presented in Figure 14. Each image was subjected to an approximate HD correction by forcing the stellar profiles to be Gaussian, there being no other calibration available. Each of the images was then registered using foreground stars, and several reference stars were collected into a row below the corresponding image of M87.

In order to observe any relative intensity variations with time in the knots along the main jet, the images were normalized such that the central galaxy and its halo were of the same amplitude. A similar analysis but normalizing the reference stars to the same amplitude was performed and is in press (Reference 9). After normalizing the halo, difference pictures in the sense of 1978 compared to 1956 were generated and are presented as Figures 15 and 16; Figure 15 is the difference between the 6-minute exposures, and Figure 16 is the difference between the 3-minute exposures. It is clear from the difference pictures that at least the inner main knot "A" has increased in brightness relative to the halo from 1956 to 1978, especially at polarization P.A. 335° .

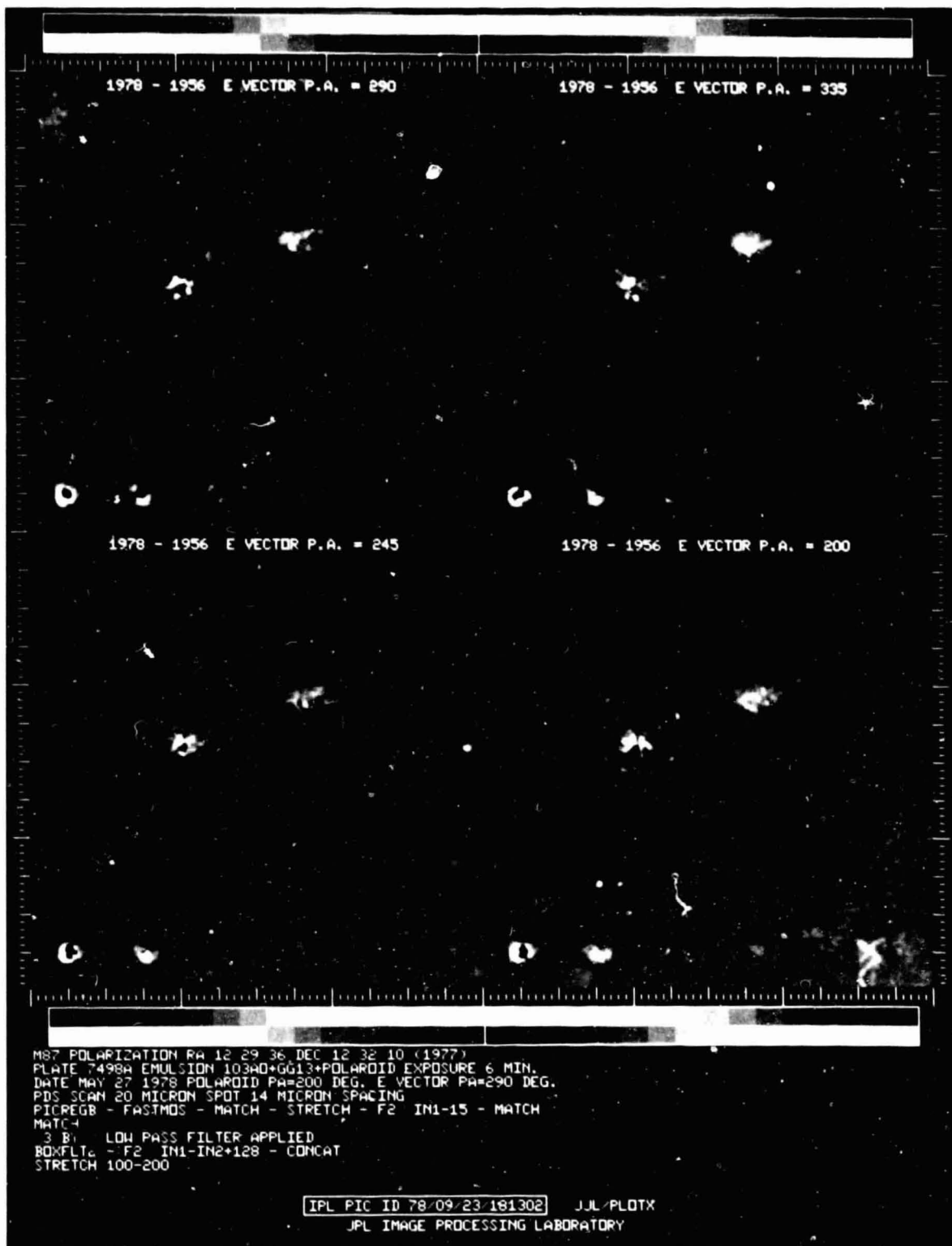


Figure 15. M87 difference images in the sense 1978 minus 1956, each in four polarization orientations. The images were scaled so that the halo of M87 matched in intensity. Reference stars appear below. These are 6-minute exposures.

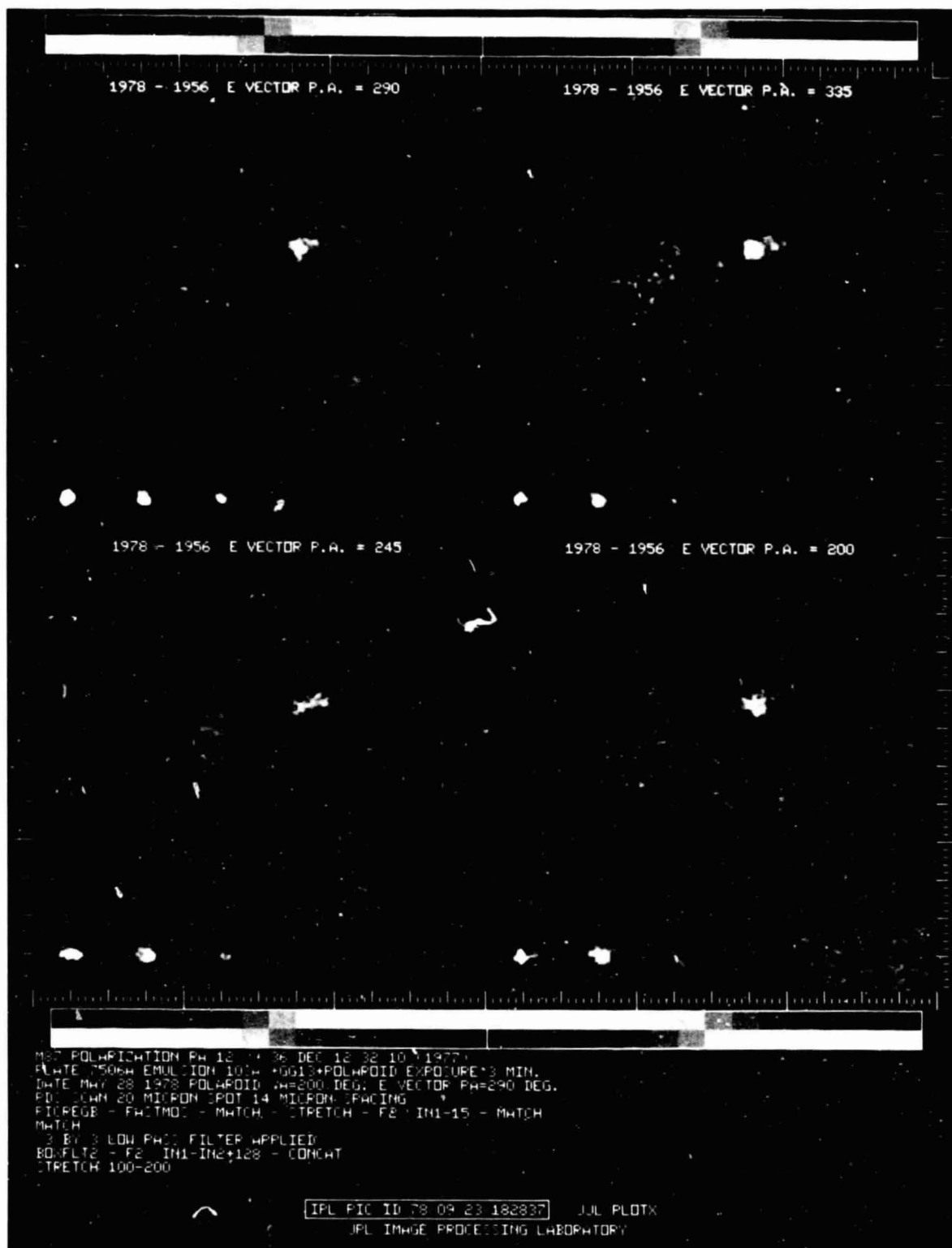


Figure 16. M87 difference images in the same format as Figure 15. These are 3-minute exposures.

SECTION V

PLANETARY NEBULAE - COMPARING EMISSION LINE IMAGES

In this section, the steps leading toward calculation of the volume emission coefficient, temperature, and electron density from emission line images of planetary nebulae are described.

The work in this section was inspired and performed by Peter Kupferman of JPL, using the facilities of the Image Processing Laboratory. Images were obtained at the Palomar 60-inch telescope with a silicon vidicon through interference filters, listed in Table 1, of three planetaries NGC7662, NGC6720, and NGC2392. The images comprised 256-by-256 pixels of 12 bits each at 0.5 seconds of arc per pixel.

Each image was radiometrically decalibrated by subtracting averaged dark current frames and dividing by averaged flat fields obtained during the observing run, implying a linear light transfer curve model. All of the images for each object were then geometrically registered using nearby reference stars unrelated to the nebula. All of the images obtained at each wavelength (there were from 2 to 9 redundant pictures) were averaged to provide a single picture at each wavelength. A low spatial frequency analytical model was generated to match the residual background sky level after decalibration. This model was subtracted from each image in order to reduce small inhomogeneities in the sky. Figure 17 illustrates a mosaic of each of the images for NGC6720 at this stage in the processing. Each image is arbitrarily scaled to produce a visible picture. Figure 18 displays the log amplitude of the Fourier transform of each of the images in Figure 17. It is evident

Table 1. Wavelengths of Each Planetary Nebula Image

Target Line I.D.	λ	Bandpass \AA ^o
[OII]	3727	20
[OIII]	4363	13
HeII	4686	28
H β	4861	15
HeI	5876	15
[OIII]	5007	17
[OI]	6300	6
Ha	6563	11
Ha+[NII]	6563	175
[SII]	6716	10
[SII]	6731	11

from these figures that a periodic pattern due to the deceleration grid in the vidicon (hash lines) and clusters due to quasi-coherent noise are still present to a varying degree in each image. From inspection of Figure 18, it was determined that the system MTF went to zero at about 0.25 cycles per sample due to atmospheric seeing; thus, it was possible to reduce the coherent, periodic, and random noise greatly by convolving with a band pass filter that suppressed information above this frequency. This technique obviated the need for a custom modification of each Fourier transform. Figure 19 displays each of the rescaled Fourier transforms after convolution, and Figure 20 illustrates the corresponding smoothed images.

In order to compute the volume emission coefficient, each image was first converted into polar coordinates (Figure 21) in which each row represents a radial section outward from the central star, the rows extending in azimuth from 0° at the top to 360° at the bottom. If one can assume spherical symmetry, then each row in the polar coordinate space would provide a separate model for the nebula, allowing different models for different structures at those azimuths. From the observed projected radial intensity profiles $I(x)$, one can obtain the true radial intensity profile $j(r)$, known as the volume emissivity from the Abel transform:

$$j(r) = -\frac{1}{\pi} \int_r^\infty \left(\frac{dI(x)}{dx} / \sqrt{x^2 - r^2} \right) dx \quad (7)$$

From the true radial emission $j(r)$, one can regenerate the nebula by using the inverse polar coordinate transformation. In Figure 22, the positive volume emission coefficient is displayed in red with negative regions coded in green. Negative emission indicates where the planetary model is not circumferentially symmetric and that a more sophisticated model is desired.

Absolute calibrations were obtained from spectrophotometry performed at specific points in the nebula at the McGraw Hill 52-inch telescope at Kitt Peak. The intensities at these points could be used to scale the digital images linearly so that each pixel was known in units of ergs/cm²-steradian-sec, providing units of $j(r)$ in ergs/cm³-steradian-sec. Relative photometry is good from 2 to 4 percent, and absolute photometry is good from 5 to 8 percent. A map of mean temperature along the line of sight can be computed from the ratio of the [OIII] lines 5007 and 4363 after Osterbrock (Reference 10, p. 100) using the relation:

$$T(K) = \frac{32900}{\log_e \left(\frac{I(5007)}{I(4363)} \right)} \quad (8)$$

This map is presented in Figure 23.

The electron density could be computed from the [SII] lines 6731 and 6716, using a table calculated by Osterbrock (Reference 10, p. 112) for an assumed temperature of 10^4 K. This map is presented in Figure 24. The bright rings are artifacts.

To illustrate the spatial distribution of material in different ionization states, the following three figures are presented. Figure 25 is a mosaic of images in different bands, each color coded green, added to H α color coded as red. The relative intensities have been adjusted to reveal the most information. In Figures 26 and 27, the ionization structure has been enhanced using the HSI transformation (Section VI) and assigning three bands to the color primaries blue, green, and red according to Table 2. The radial position of each ionization shell is apparent.

Table 2. Color Assignments of Narrow Band Images for Figures 26 and 27

Figure	Color Primaries		
	Blue	Green	Red
26	HeII, 4686	HeI, 5876	[OI], 6300
27	[OII], 3727	[OIII], 5007	[OI], 6300

These techniques should be applicable to any objects in an optically thin, non-LTE environment.

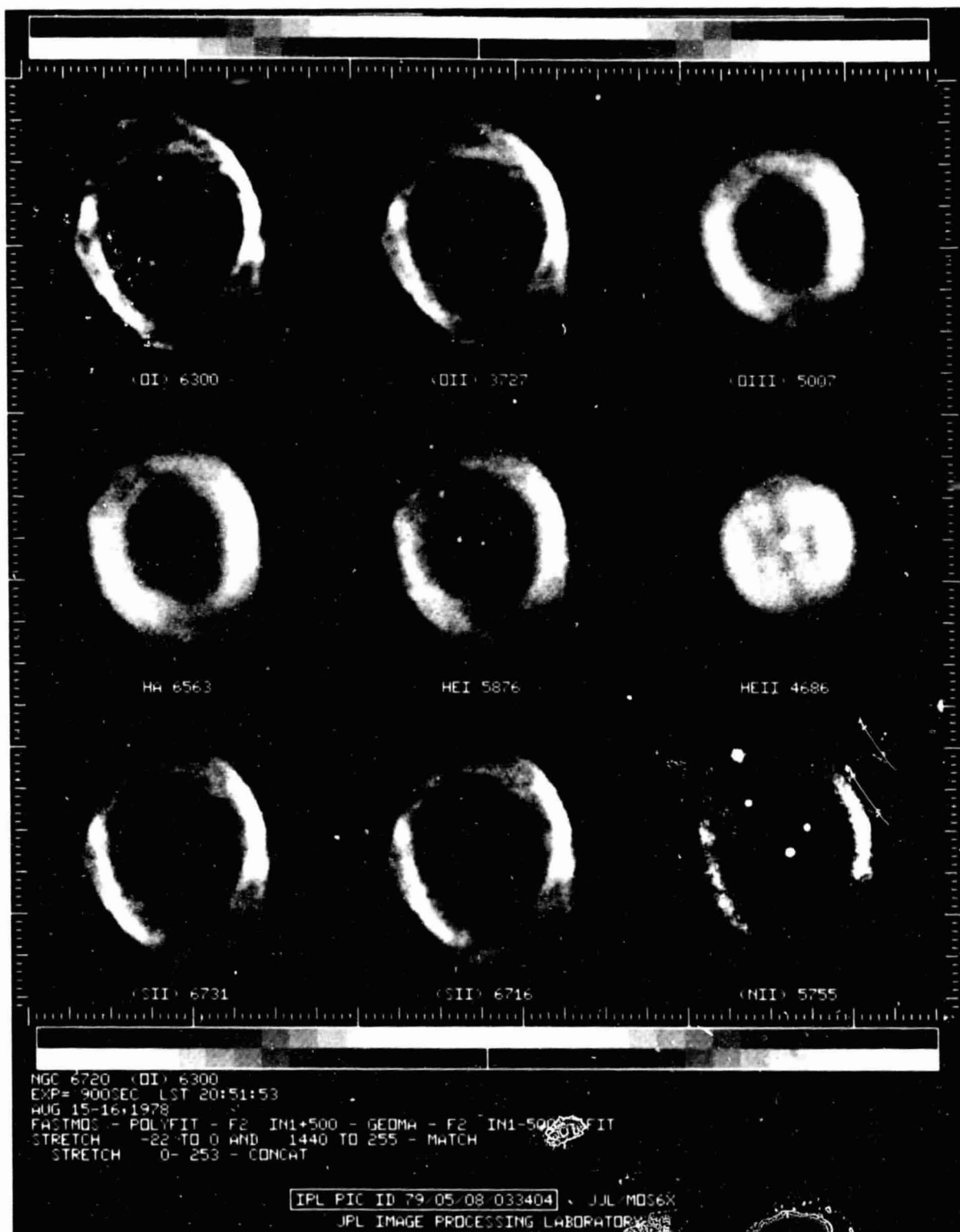


Figure 17. NGC6720 mosaic of nine emission line images after radiometric correction and scaling for visual interpretation. Coherent, periodic, and random noise is clearly a problem in several of the images.

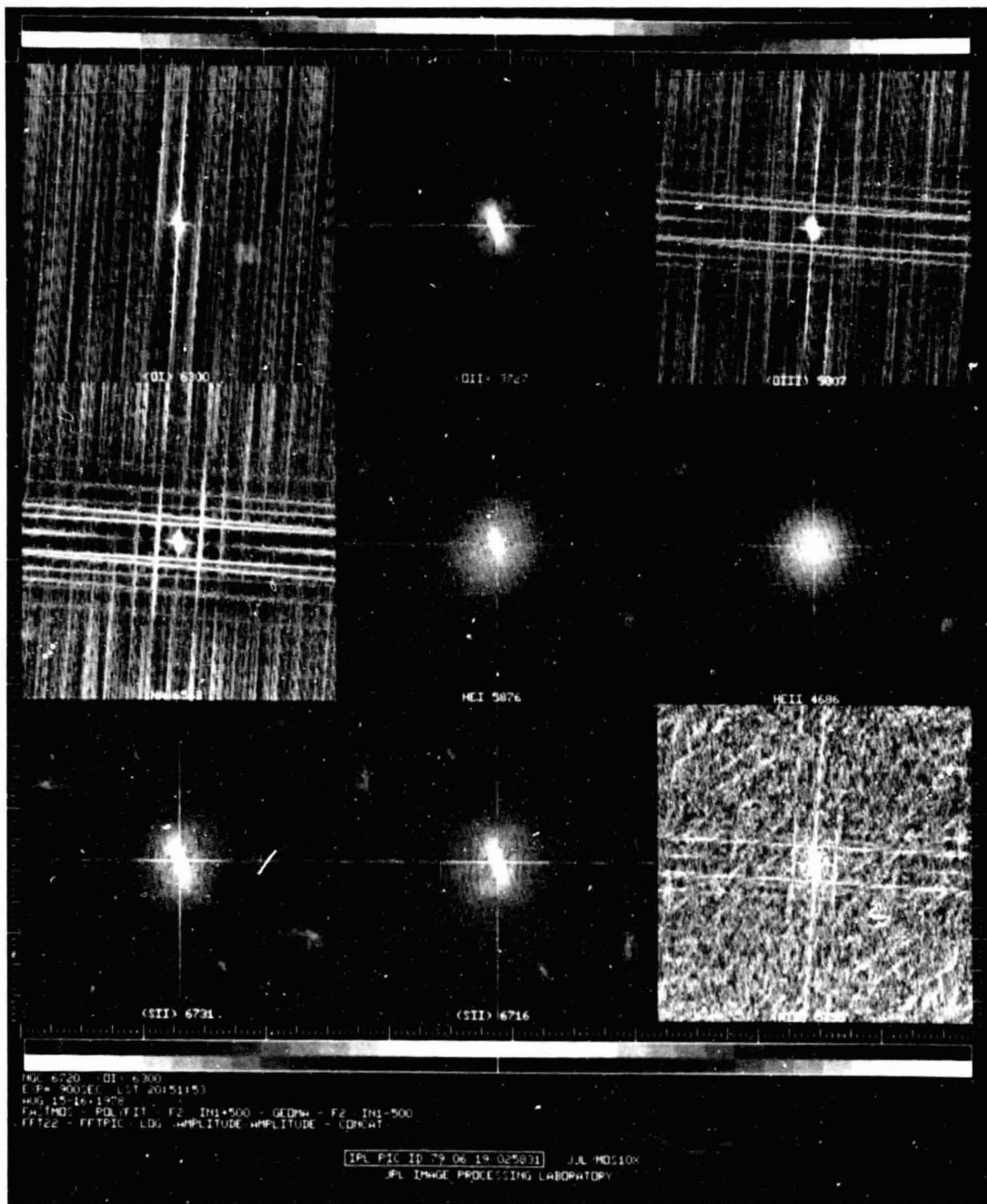


Figure 18. NGC6720 two-dimensional Fourier transforms displayed as log amplitude in a one-to-one correspondence with the images of Figure 17. The object data populates only the central region of each transform. Coherent noise is seen as clusters and periodic noise as streaks.

ORIGINAL PAGE IS
OF POOR QUALITY

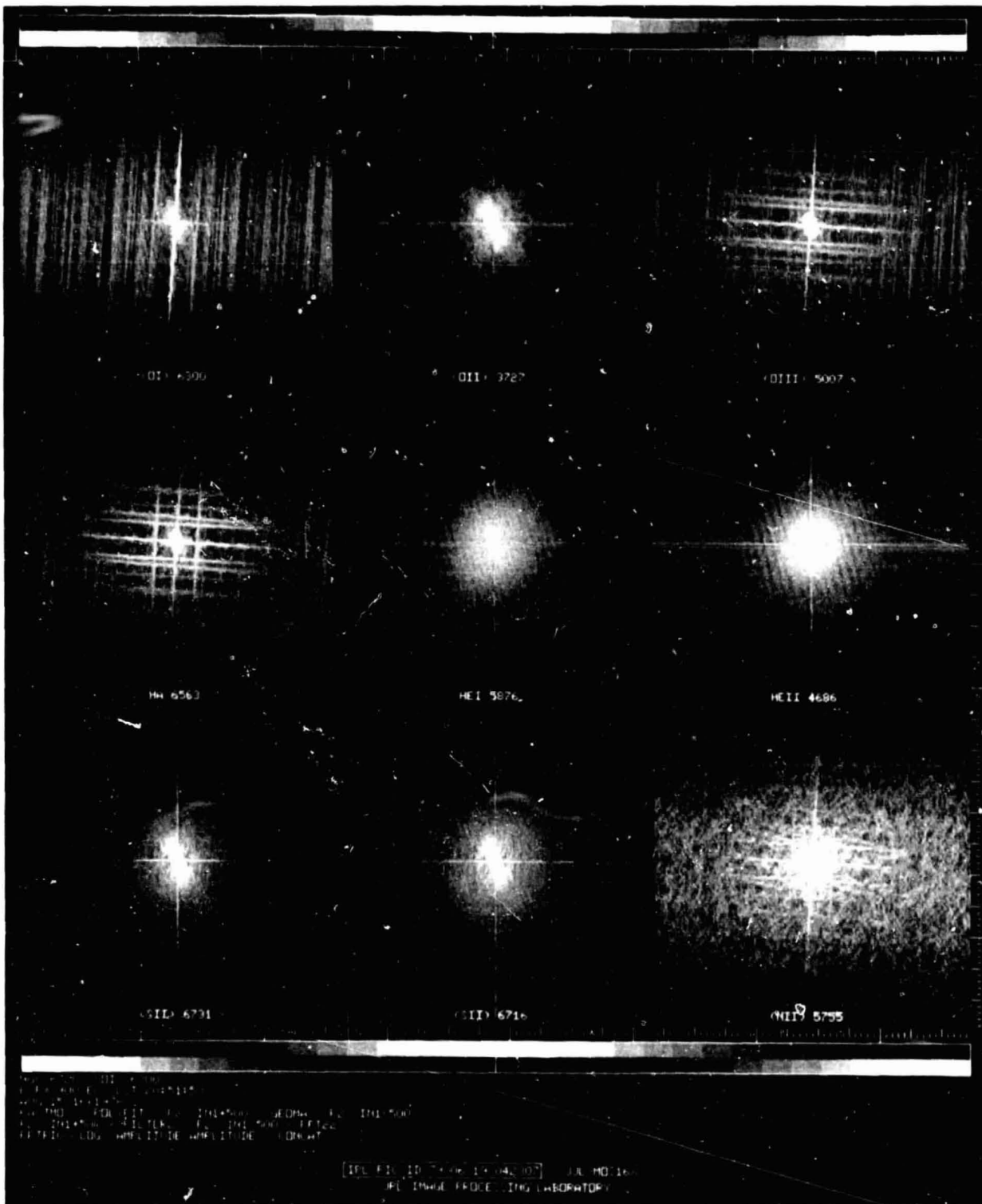


Figure 19. NGC6720 mosaic of modified transforms in the same format as Figure 18. The coherent noise spikes have been greatly reduced. Each display has been renormalized to reveal noise residuals.

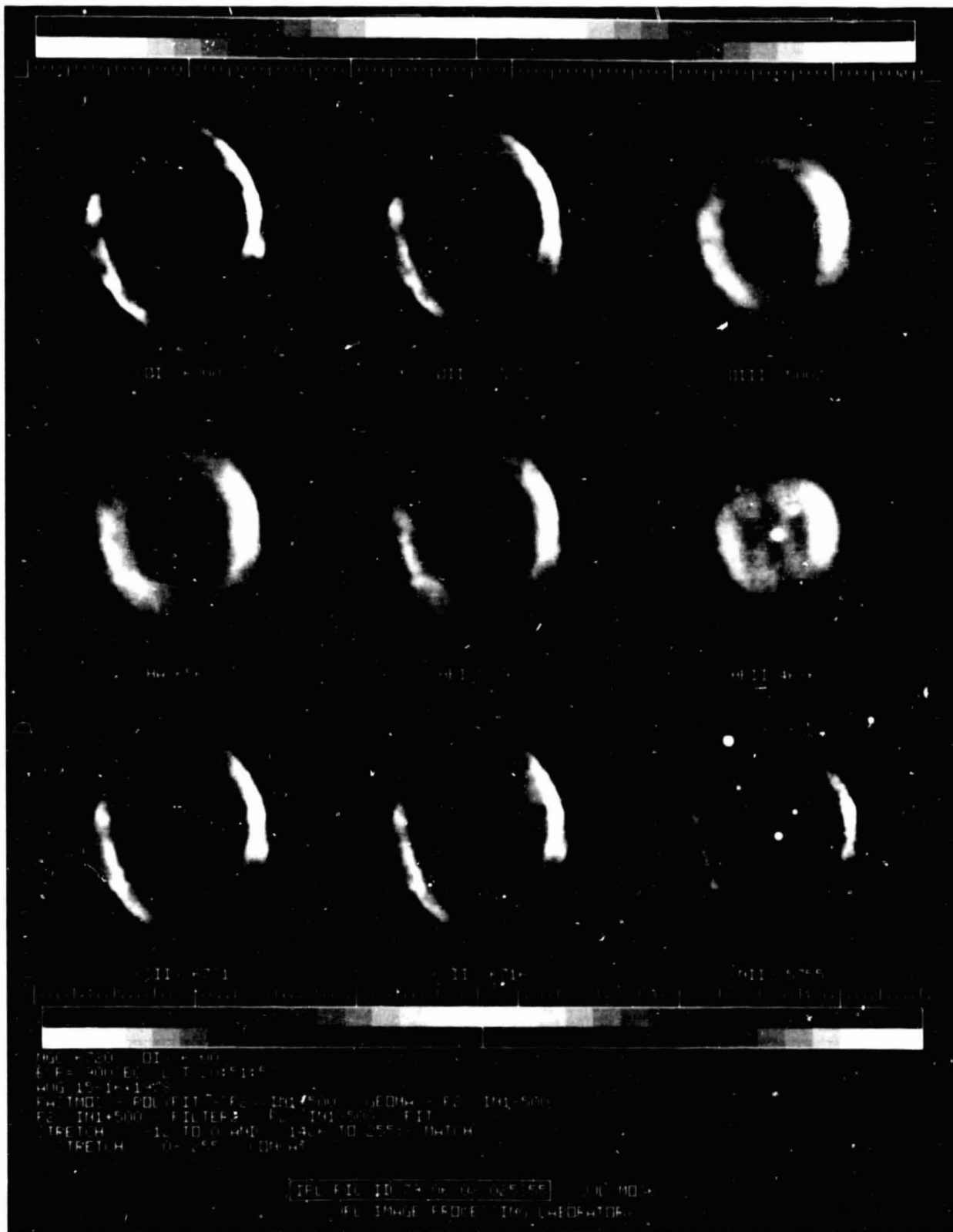


Figure 20. NGC6720 mosaic in the same format as Figure 17 after the reduction of all noise sources

5-7

ORIGINAL PAGE IS
 OF POOR QUALITY

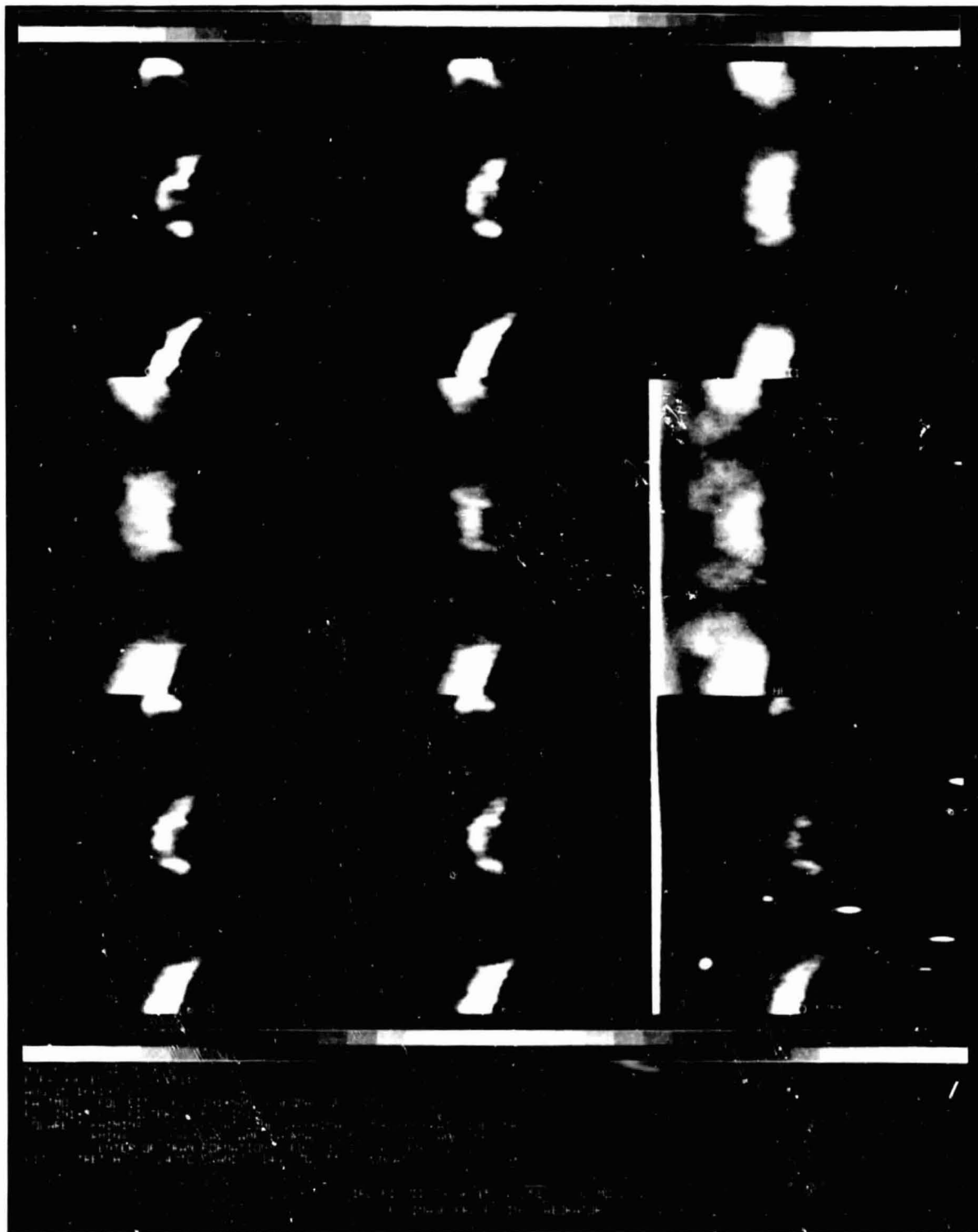
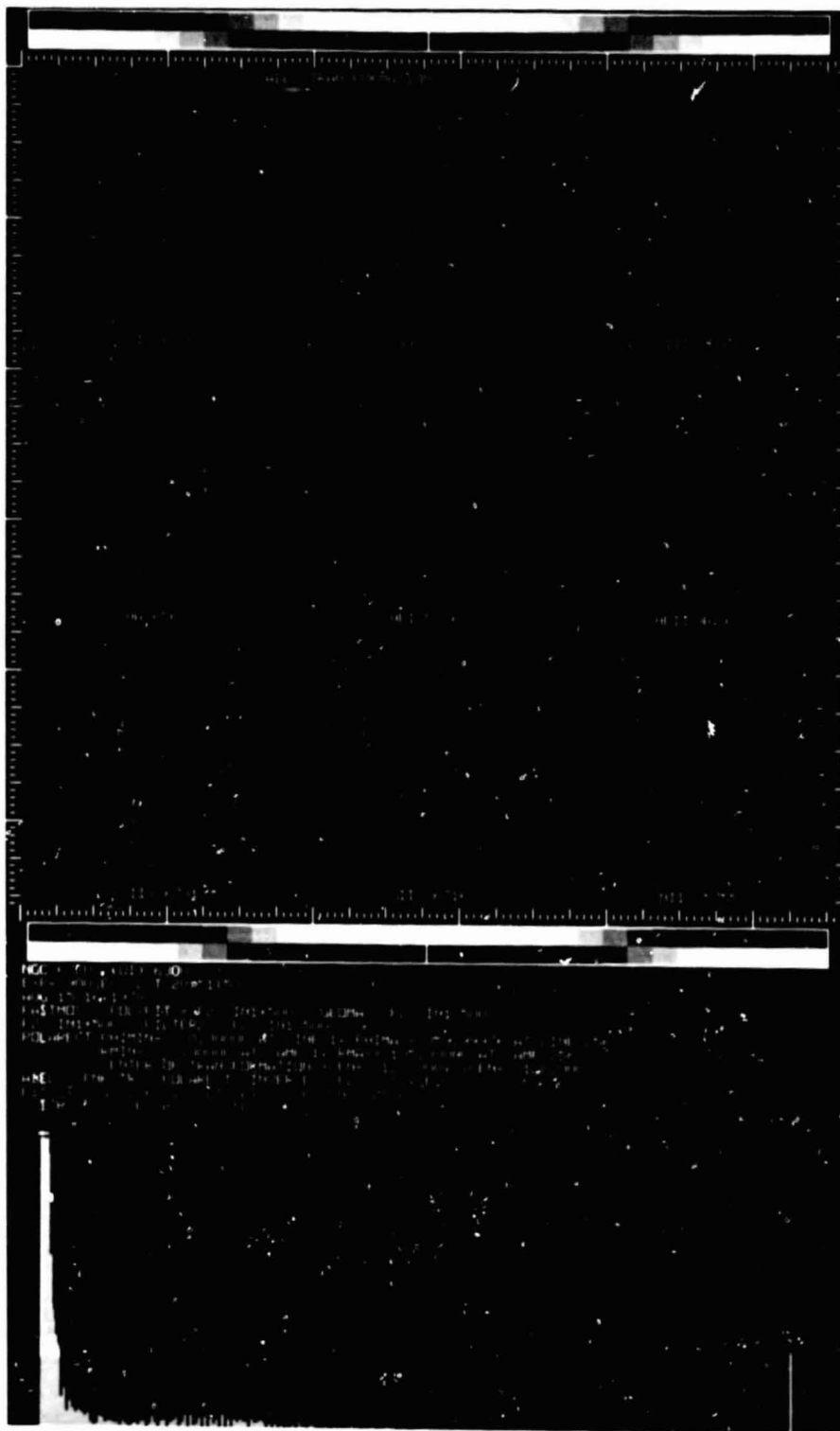


Figure 21. NGC6720 mosaic of polar coordinate transformations in the same order as Figure 20. Radial sections from the central star outward map as horizontal lines in this figure. A round nebula would appear as a vertical structure in this format.



ORIGINAL PAGE IS
OF POOR QUALITY

Figure 22. NGC6720 mosaic of the volume emission coefficient at different wavelengths suitably scaled for viewing. Positive values are coded red and negative values coded green. Negative emission is artifact caused by assumptions of spherical symmetry at each azimuth.

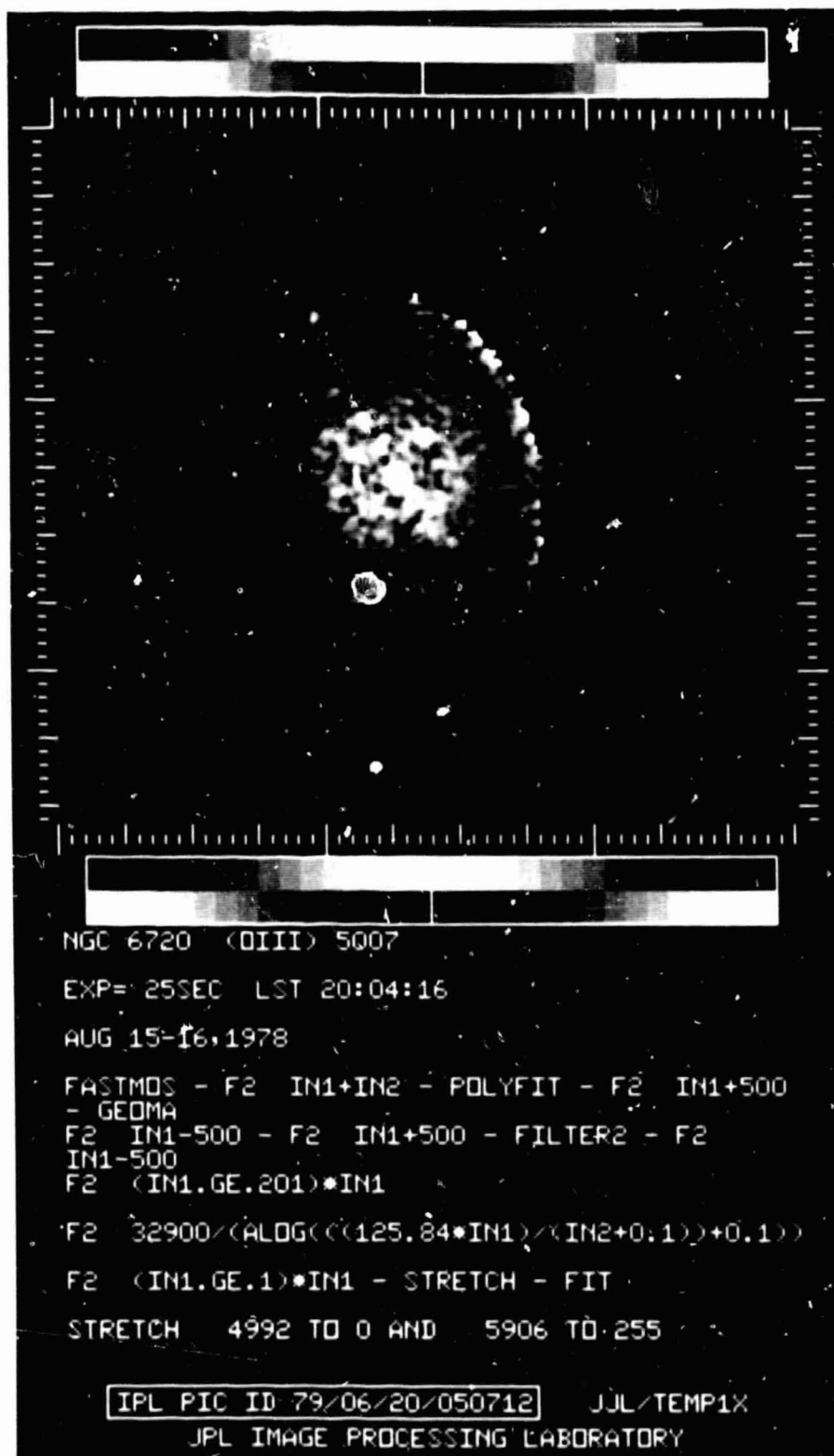
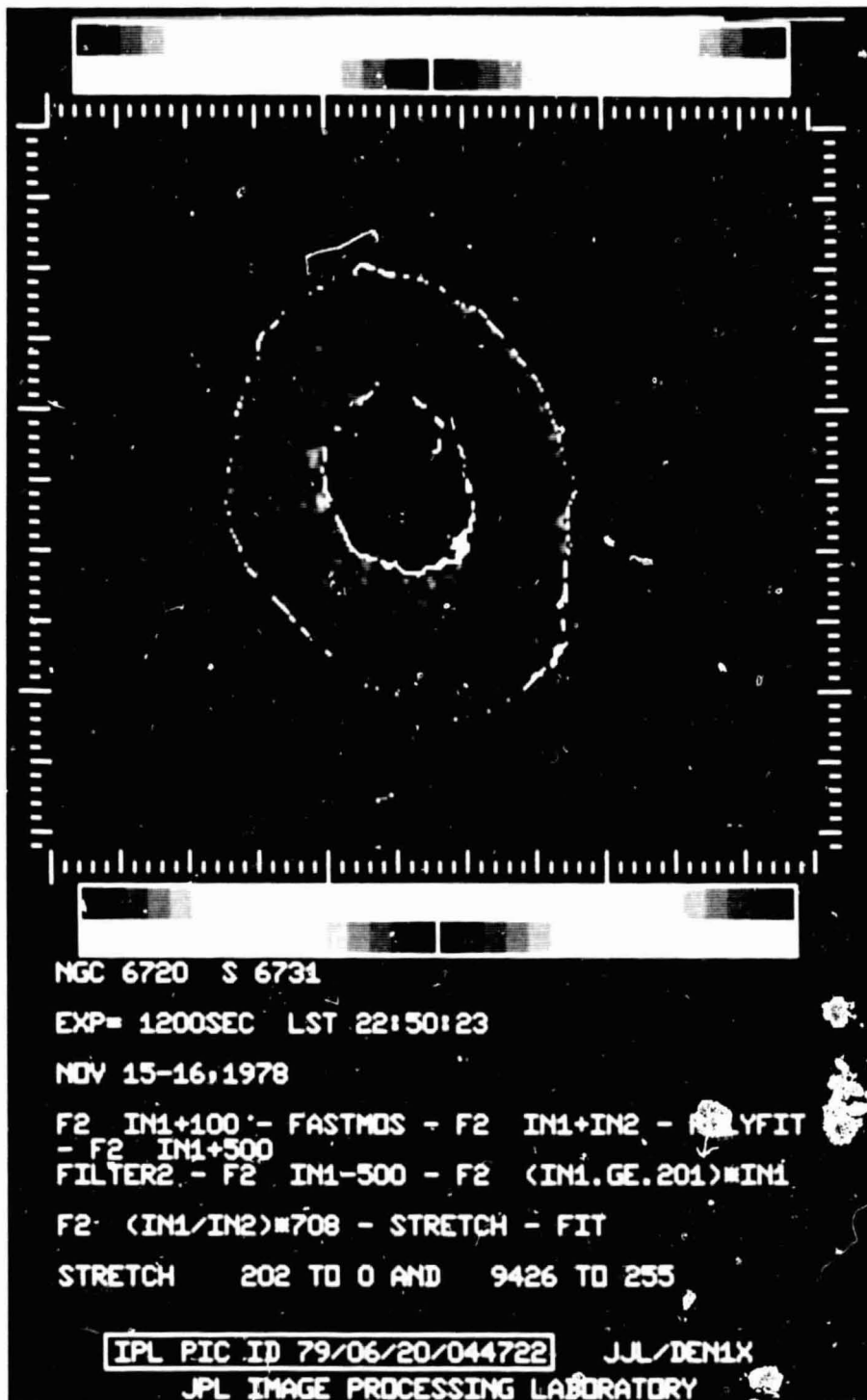


Figure 23. NGC6720 temperature map scaled for viewing. The sky was thresholded to zero because there the ratios of the [OIII] images at 5007 Å and 4363 Å are undefined.



ORIGINAL PAGE IS
 OF POOR QUALITY

Figure 24. NGC6720 electron density map scaled for viewing. The sky was thresholded to zero because there the ratios of the [SII] images at 6716 A and 6731 A are undefined.

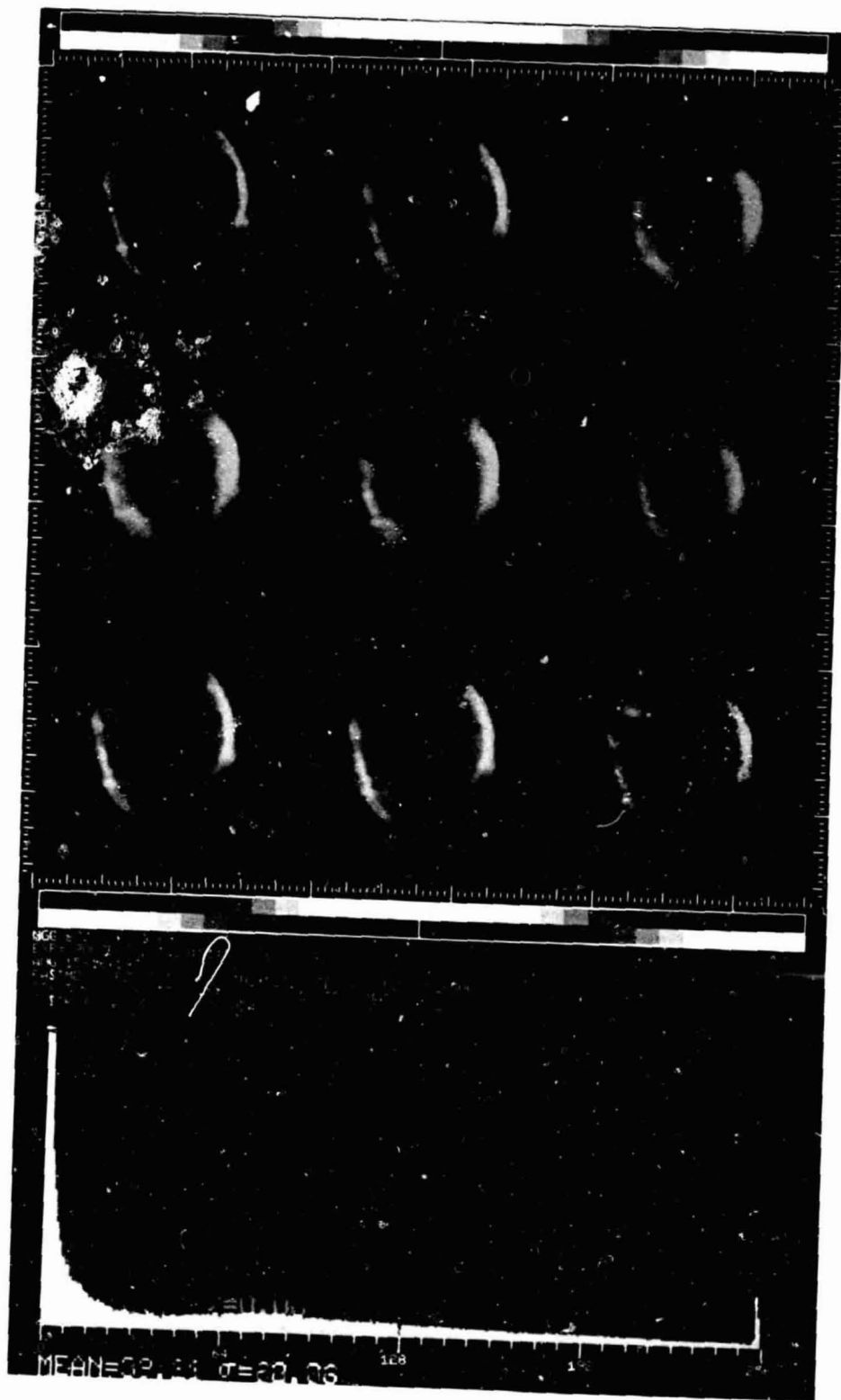
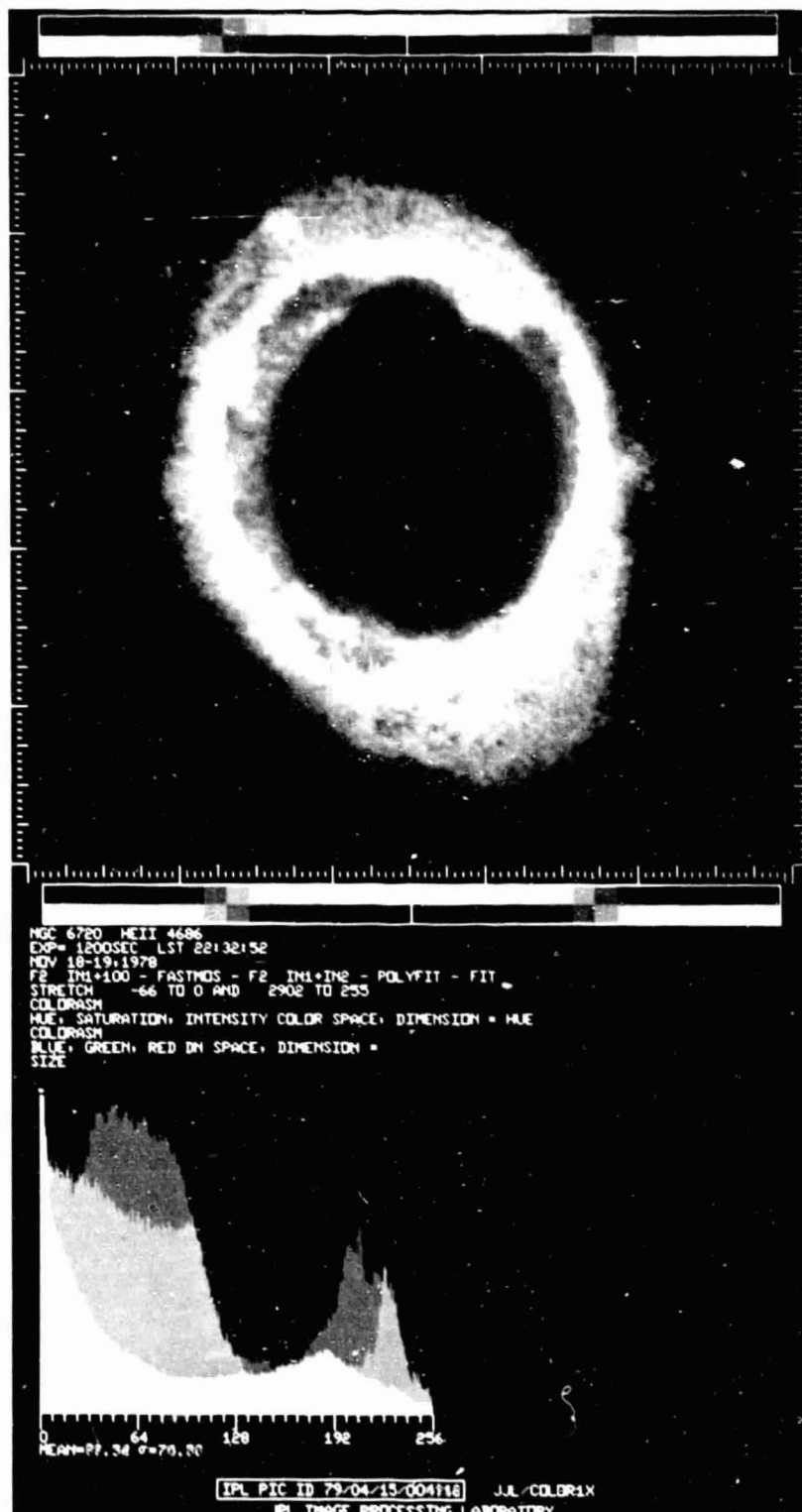


Figure 25. NGC6720 mosaic of different images color coded green and added to the H α image coded red. Intensities have been adjusted for viewing. The spatial distribution (in projection) of emitting material is evident.



ORIGINAL PAGE IS
 OF BEST QUALITY

Figure 26. NGC6720 color-coded rendition of ionization structure. Color assignments are blue = HeII, 4686; green = HeI, 5876; red = [O I], 6300. Colors have been enhanced using the HSI transformation.

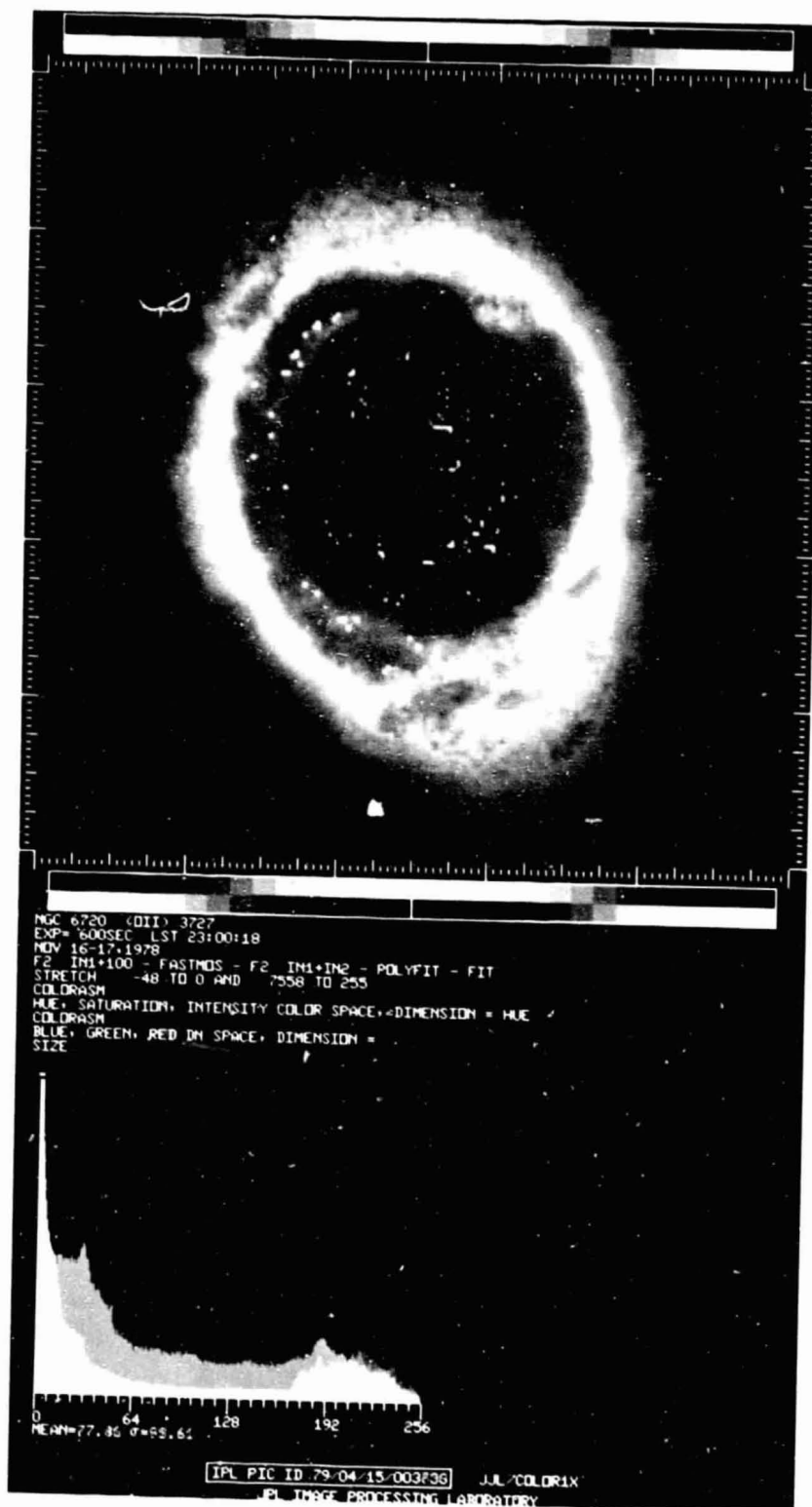


Figure 27. NGC6720 color-coded rendition of ionization structure. Color assignments are blue = [OII], 3727; green = [OIII], 5007; red = [OI], 6300. Colors have been enhanced using the HSI transformation.

SECTION VI

COLOR ENHANCEMENTS

In Sections IV and V of Reference 1, two powerful tools were illustrated for enhancing color differences between multispectral images of the same object. In this section, these two techniques (the HSI and Principal Component transformation) will be developed further and a third technique introduced, called the Log Intensity transformation. All of the images in this section were obtained from Dr. Allan Sandage of Hale Observatories. The images consisted of four spectral bands, 103a0 + WG2, 103aD + GG14, 103aE + RG1, 103aE + H α , of M82 obtained at the 200-inch telescope. The 103a0 image was synthesized from the average of four separate exposures, each registered and histogram matched. No correction was applied for the HD curve of the emulsion. Each image was linearly scaled so that the sky level was equal and the variance of the image within the region of the galaxy was also equal (this is equivalent to equating the volumes under the power spectra, thus forcing the information content of each band to be the same). The latter constraint is certainly not a real one, but it provides a good basis for analysis because each image will be represented equally, none being dominated by brighter ones.

In the remainder of this section, each of the three techniques will be applied to the same M82 images so that a comparative evaluation is possible.

A. LOG INTENSITY STRETCH

It is possible to vary the dynamic range of a set of multispectral images in any fashion whether it be linear or nonlinear and to preserve the color information (saturation and hue) by operating upon the intensity information only. In this application, it was convenient to reduce the dynamic range of the images such that they could be represented in 8 bits per pixel, a format compatible with the HSI and Principal Component transformations (and within the range of playback devices) to be addressed later. Because the majority of the galaxy resided at low intensities, a logarithmic compression was selected to reduce the upper dynamic range more than the lower dynamic range. Rather than take the logarithm of each pixel in turn (with disastrous consequences on the color) the logarithm was taken of the sum of each color band at each pixel, providing a scalar which could in turn be applied to that pixel location on each picture.

$$I'_j = I_j C_1 \log C_2 \frac{\sum_{i=1}^n I_i}{C_2 \sum_{i=1}^n I_i} \quad j=1,2,\dots,n \quad (9)$$

I_j represents the intensity of band j of n bands at one pixel, and C_1 and C_2 are constants which control the scaling and linearity respectively.

Figure 28 illustrates four color combinations of M82 obtained by selecting the original four bands, three at a time. The color assignments are listed in Table 3, and details of the emulsion and filter combinations are shown in Table 4.

Table 3. Standard Color Assignments for the M82 Mosaics

Quadrant	Color Primaries		
	Blue	Green	Red
Upper left	103a0	103aD	103aE
Upper right	103a0	103aD	Ha
Lower left	103a0	103aE	Ha
Lower right	103aD	103aE	Ha

Table 4. Emulsion/Filter Combinations

Emulsion	Filter
103a0	WG2
103aD	GG14
103aE	RG1
103aE	Ha

Figure 28 consists of the original intensity images. One can distinguish much structure at the center of the galaxy, but not much is visible at lower intensities. Figure 29 illustrates the same mosaic as Figure 28, but after the Log Intensity transformation. Contrast is much lower along the bright bar but lower intensities are more readily observed. The color playback device can be operated under several calibration conditions. In the case of Figures 28 and 29, the device produced a print where equal steps in intensity in each band mapped into equal density steps in the photographic negative. This produces a pleasing dynamic range, segregates well between intensity levels in the print, but allows some cross talk between the colors so that hue becomes a function of intensity. Figure 30 is identical with Figure 29 except that the playback device was calibrated to produce a print where the reflectance of each step of the gray scale in each band (blue, green, or red) is proportional to the intensity of that band. This requirement provides an additional logarithmic compression effect, enhancing the lower intensity range. Colors should be truer in Figure 30 than in Figure 29. Both versions will also be presented later to aid in interpretation. Note

that the Log Intensity stretch has not produced a significant alteration of the colors in the scene; it acts as a means of redistributing intensity information only. Considerable filamentary detail can be seen in Figure 30, detail that remains invisible in Figure 28.

B. HSI

The HSI or Hue, Saturation, and Intensity transformation was introduced in References 1 and 11 where it was used to enhance color differences in NGC1097. Briefly, this transformation attempts to mimic the physiological parameterization of the color space from a polar coordinate transformation in which intensity is the sum of the three spectral bands (blue, green, and red), saturation is the colatitude from the gray axis, and hue is the longitude about the gray axis. In this section, the HSI transformation will be applied to M82 as a comparison with the Principal Component transformation in the next section, but also to illustrate some further manipulations of the HSI space.

The images input to the HSI space are in this case the products of the Log Intensity transformation rather than the intensities themselves. Figure 31 illustrates a mosaic of the four spectral bands produced by the Log Intensity process, in the order upper left = 103a0, upper right = 103aD, lower left = 103aE, and lower right = Ha. Subsequent color products will be combinations taken three at a time as in Table 3. The HSI processing consists of first generating the Hue, Saturation, and Intensity pictures from the blue, green, and red inputs. This is followed by performing a nonlinear contrast enhancement upon the Saturation picture so that the output histogram is equally populated everywhere. An optional step is introduced consisting of performing a low pass filter upon the histogram of the Hue picture and then nonlinearly contrast enhancing the Hue picture so that the Hue histogram would resemble the low pass filtered version. This last operation, although at first obscure, has a simple function. Concentrations of values in the Hue histogram are caused by regions of the pictures which have the same mean wavelength (the pattern recognition definition of an object "class"). It would be desirable to perform a higher than normal contrast enhancement in these regions of the Hue histogram in order to improve the discriminability of the eye to color differences within a single "class" of object which, because of the clustering of values, probably contains a great deal of information. This selective contrast enhancement is performed by first low pass filtering the Hue histogram, a process which smears or broadens the histogram clusters, and then using this histogram as a model for the desired output histogram. The contrast enhancement table generated to achieve the desired output histogram is highly nonlinear but is still monotonic so that crossovers of color are forbidden. Several advantages of this enhancement technique are that the filter preserves the means of the clusters; thus, the mean wavelength (mean hue) of the clusters is unaltered and the enhancement can be performed automatically.

Figures 32 through 35 illustrate various stages in the above process for each of the four combinations of three colors selected as indicated in Table 5.

Table 5. Assignments of Bands to Primaries in Figures 32 through 35

Figure	Color Primaries		
	Blue	Green	Red
32	103a0	103aD	103aE
33	103a0	103aD	Ha
34	103a0	103aE	Ha
35	103aD	103aE	Ha

In each figure, the left column consists of three pictures in the following order: top is blue, middle is green, and bottom is red after the saturation and hue enhancements. These can be compared with the corresponding unenhanced versions in Figure 31. The right column in these same figures consists of enhanced HSI images in the following order: top is hue, middle is saturation, and bottom is intensity. The histograms at the bottom of the left column correspond one to one with the original unenhanced versions of the pictures above them. At the bottom of the right column of pictures are two columns of histograms. These are in order from top to bottom: hue, saturation, and intensity; the left column represents the original histograms before enhancement and the right column after enhancement.

Spikes every 60° in the hue histogram are artifacts due to coincidences of planes of constant hue with the three-dimensional lattice of 8-bit color space. These spikes confuse the operation of the hue contrast enhancement and reduce its effectiveness.

Color reconstructions based upon contrast enhancements of the saturation only (no modification of the hue) are presented in Figures 36 and 37 in the order of Table 3. The modified hue images require careful interpretation and thus are not shown as color reconstructions. Figure 36 is calibrated with equal intensity steps corresponding with equal density steps and Figure 37 has equal intensity steps as equal reflectance steps as previously discussed. Considerable color structure is visible, betraying the spatial distribution of features with similar spectral properties.

For some analyses, the intensity and saturation of a scene proves to be a nuisance. In order to see the mean wavelengths residing everywhere in the scene, the inverse HSI transformation was performed as usual except with both the intensity and saturation images discarded. This product is presented as Figure 38 in the usual Table 3 format. Some regions of the image which were too bright or dark to register color before are now visible. The sky is quite complex in hue because it has been raised above where the true sky level should be in order to observe faint structure, resulting in random noise of all spatial frequencies

dominating the color. The hue of a pixel with either an intensity or a saturation of zero is undefined.

C. PRINCIPAL COMPONENT

The Principal Component transformation was introduced in Reference 1 as a means of discriminating color structure without necessarily color coding it in a way traceable to the true color. A method has been developed (Reference 12) which allows a reconstruction of the approximate colors of a scene after enormous color exaggeration. The method does allow some cross talk between color channels and is thus dangerous to use if no care is taken in its analysis, but the technique provides the most powerful enhancement available. The reasons for this can be considered advantageous or disadvantageous depending upon one's point of view. The reasons are as follows:

- (1) The algorithm performs equally well in discriminating color differences even if the images are not properly intensity balanced to begin with.
- (2) The technique is not limited to three colors, but can operate in a space of dimensionality N where $N > 2$.
- (3) The process is entirely automated, deriving the optimal transformation from diagonalizing the covariance matrix, a statistical quantity computed from the images.
- (4) The process formats images in order of descending information content, allowing manipulation of intermediate products.

Briefly, the Principal Component transformation consists of determining that linear transformation (R) between the images which solves the set of matrix equations:

$$R^t K R = K' \quad (10)$$

where K is the covariance matrix of the pictures, t means transpose, and K' is the matrix whose diagonal elements are the eigenvalue solutions to the characteristic matrix of K . The enhancement process consists of determining the transformation matrix (R) and then of transforming the different spectral bands with this matrix into uncorrelated images.

A mosaic of the uncorrelated images is presented as Figure 39. The histograms below match one to one with the images above them. Considerable detail is evident in these images and it was at this stage that the application of this technique stopped in Reference 1. Table 6 gives the eigenvalues for each of the images of M82 in Figure 39. The eigenvalues represent the variance or information content in each image.

Table 6. Information Content in Each Principal Component Image of M82 for Figure 39

Quadrant	Eigenvalue
Upper left	4414
Upper right	679
Lower left	71
Lower right	33

In order to understand the nature of the images of Figure 39 better, the transformation matrix which generated them is presented.

$$\begin{pmatrix} \text{Upper left} \\ \text{Upper right} \\ \text{Lower left} \\ \text{Lower right} \end{pmatrix} = \begin{pmatrix} 0.5118 & 0.5241 & 0.5070 & 0.4543 \\ -0.4578 & -0.3456 & 0.0901 & 0.8141 \\ -0.7136 & 0.4792 & 0.4469 & -0.2474 \\ 0.1377 & -0.6132 & 0.7315 & -0.2639 \end{pmatrix} \begin{pmatrix} 103a0 \\ 103aD \\ 103aE \\ H\alpha \end{pmatrix} \quad (11)$$

For example, from the matrix, one can see that the upper right image is equivalent to $H\alpha$ minus the average of 103a0 and 103aD, and that the upper left image is essentially the intensity transformation or sum of each image weighted by how well it correlates with the average.

The color enhancement consists of contrast enhancing the principal component images using a nonlinear enhancement which fills the output histogram so that it has a gaussian distribution, and then performing the inverse transformation using (R^t) back to a recognizable color space. In order to understand this process, it is important to visualize the color space. Because the original input images are highly correlated, the majority of the color space (N-dimensional histogram) is populated along and around the gray axis, leaving empty that portion of the space far from the blue = green = . . . = red diagonal. Contrast enhancements upon the individual color bands assure that the entire diagonal is populated but it does little to populate off-axis regions of the color space. The Principal Component transformation performs a rotation of the color space such that what was once the gray axis (or the major information axis) now lies along one of the new axes, each new axis in turn being assigned an orthogonal direction through decreasingly smaller axes of the color space population until all degrees of freedom are exhausted. One can now see that the first principal component image is the intensity (upper left of Figure 39) because it coincides with the longest or intensity axis of the color space distribution. The narrowest axis through this distribution (lower right of Figure 39) is the least of all correlated directions and contains the least information and the most noise. Once the main axis of the color distribution has been aligned along a new coordinate direction, a contrast enhancement in the other coordinate direction (other pictures in Figure 39 than

the upper left) fills the color space. The inverse transformation using (R^t) re-rotates the color space to its original orientation such that blues return approximately to blues, etc. In the case of M82, all four bands were processed simultaneously in this fashion and the retransformed images were selected in groups of three for color addition in a manner similar to Table 3. Figure 40 illustrates the mosaic. Considerable color structure can be seen in the filaments.

To reduce the noise level, each of the Principal Component images except the intensity image (upper left of Figure 39) was filtered using a two-dimensional median filter of a dimension which increased as the information content, given by the eigenvalue, decreased. Upon retransformation, the color-recombined products shown in Figure 41 appear softer and much less noisy. The equivalent operation performed upon the individual color bands would have severely degraded the galaxy in order to reduce the noise an equivalent amount.

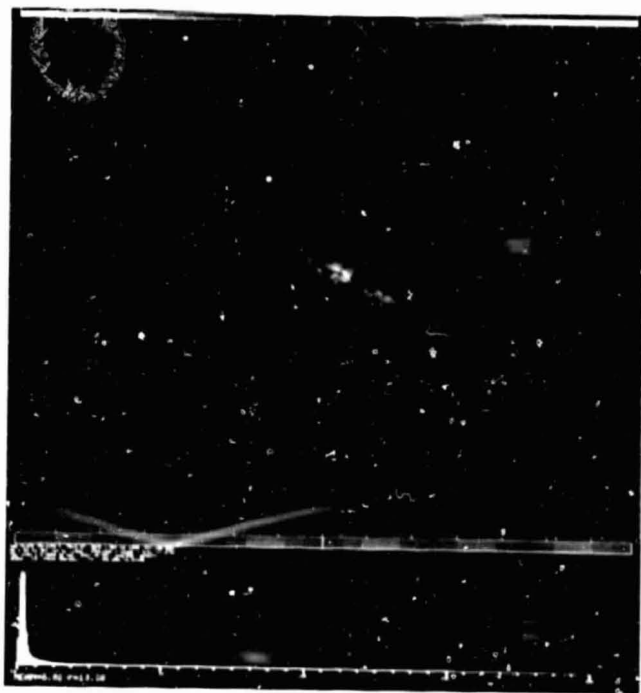
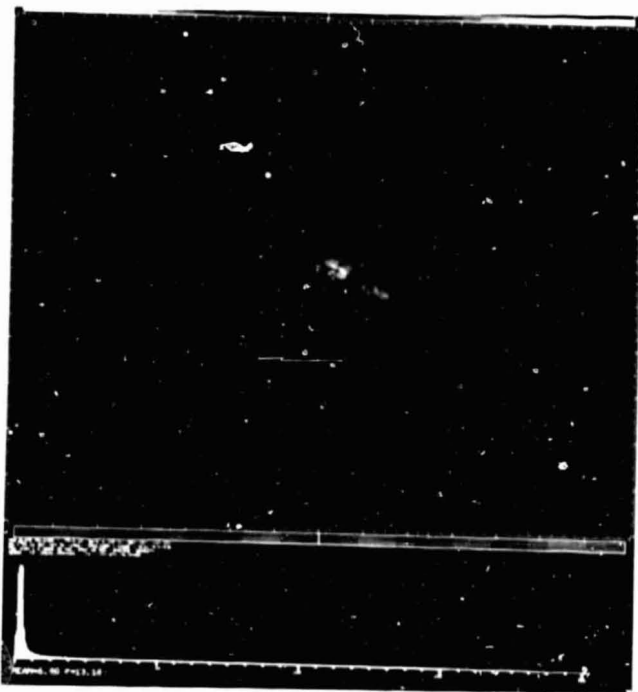
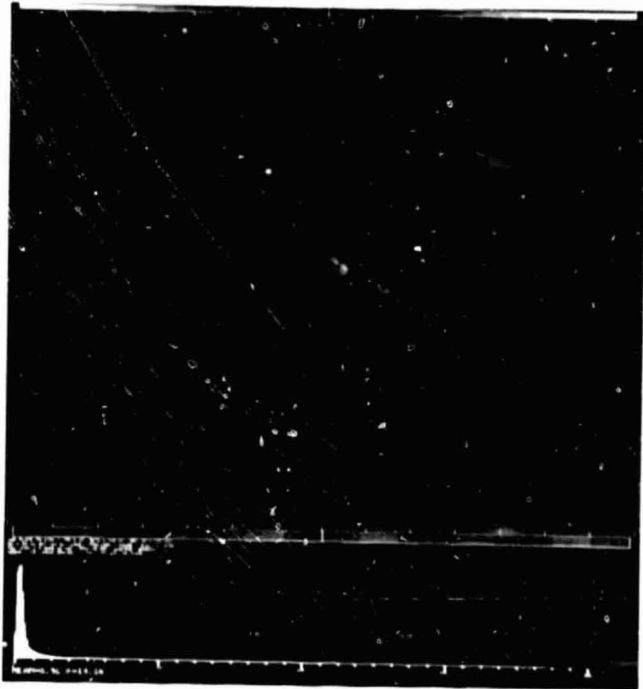
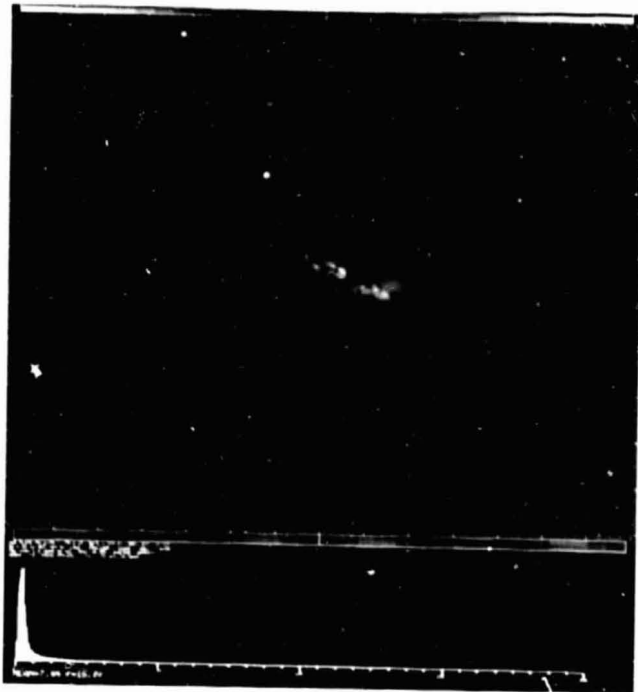


Figure 28. M82 mosaic of four combinations of three colors each. The images represent intensity information coded as equal density steps. All of the M82 mosaics appear in the order of Table 3 in the text. The histograms below are of the sums of all three images.

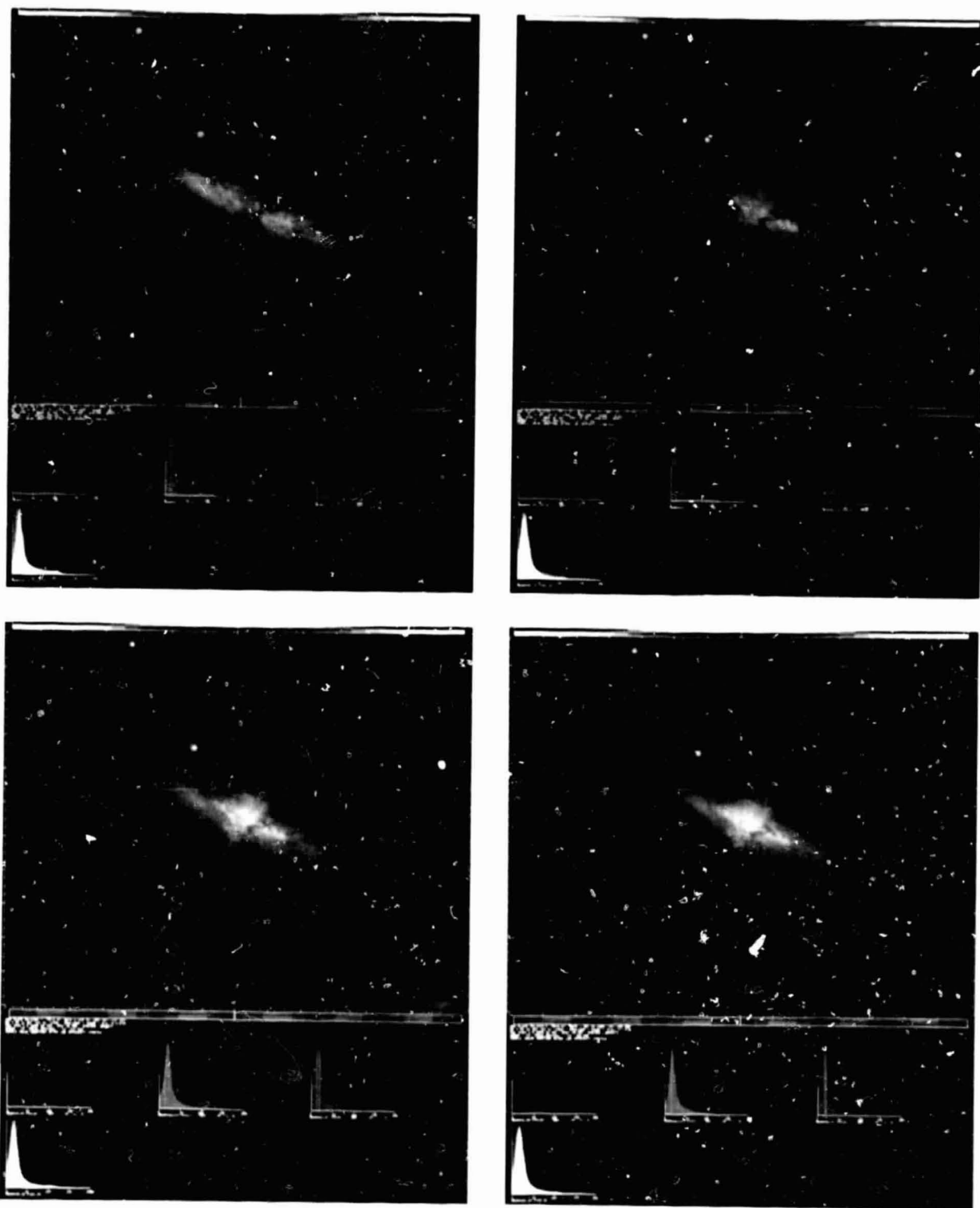


Figure 29. M82 mosaic after the Log Intensity transformation which preserves but does not enhance color differences. Images are coded so that log intensity is in equal density steps. See Table 3 for color designations. The histograms are color coded for each spectral band assignment. The lower left histogram is the sum of the ones above it.

ORIGINAL PAGE IS
OF HIGH QUALITY

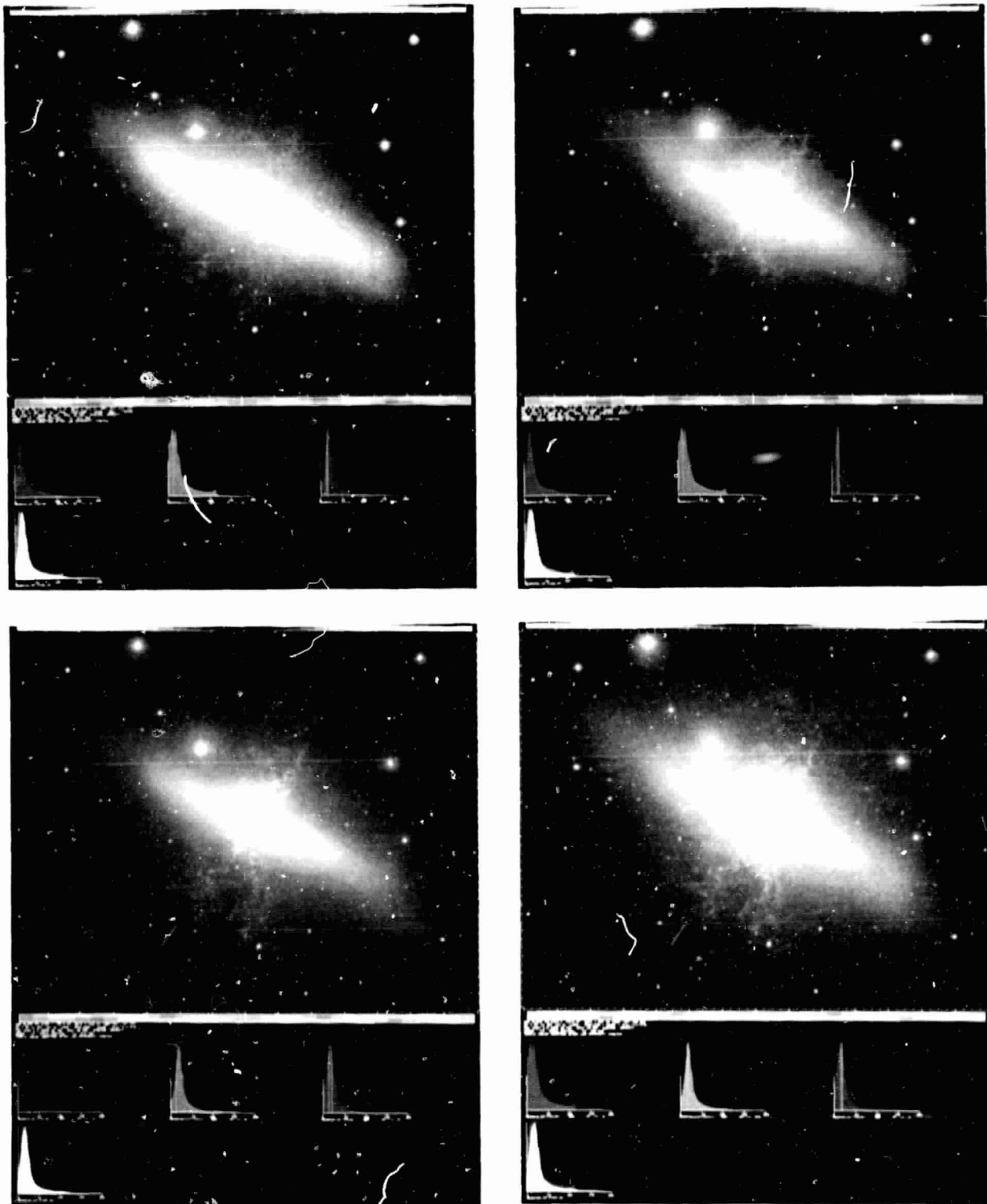


Figure 30. M82 mosaic after Log Intensity transformation but coded with log intensity in equal reflectance steps. This implies a further logarithmic compression. See Table 3 for color designations. Filaments are readily visible in this version. Histograms are the same as for Figure 29.

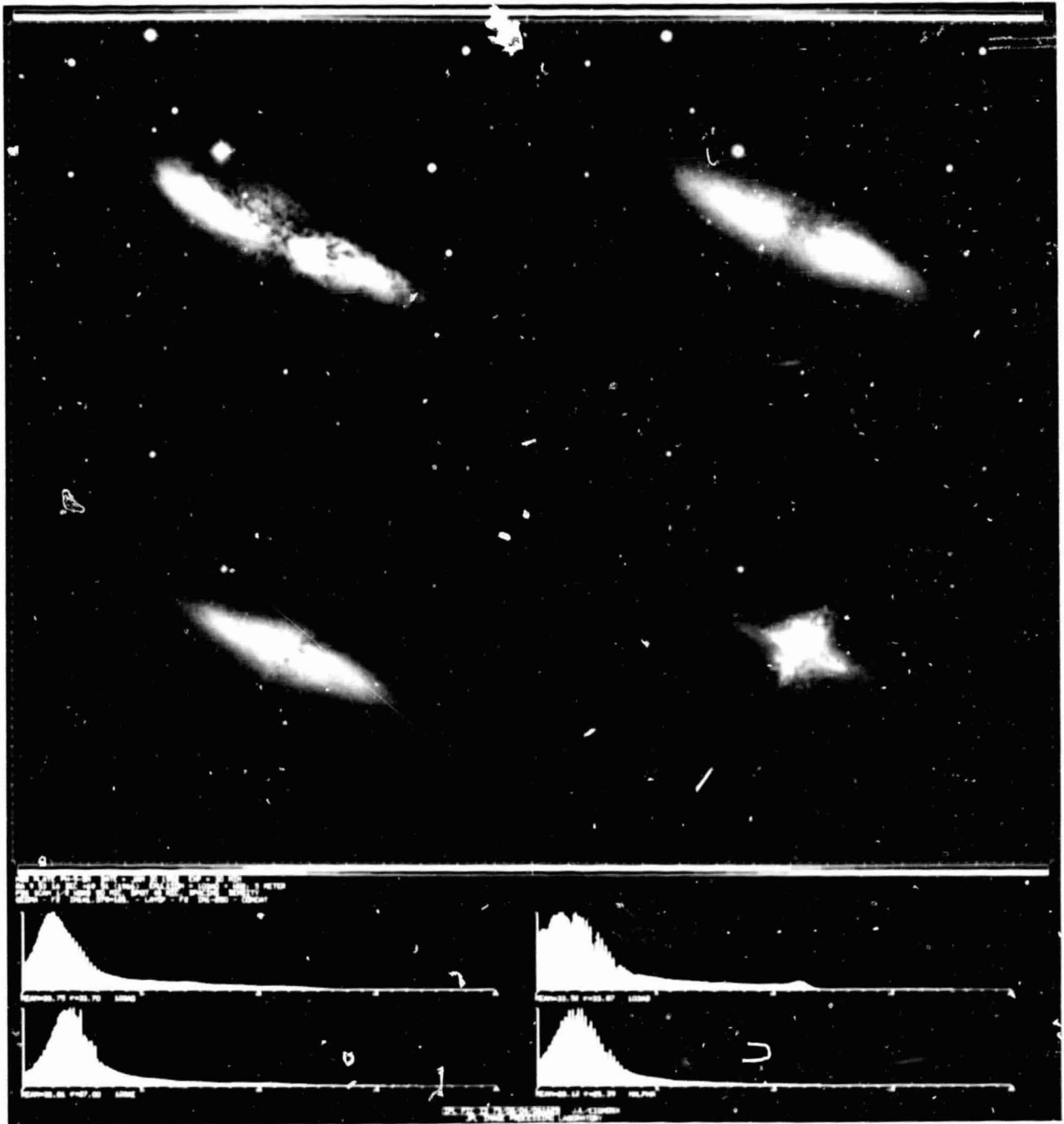


Figure 31. M82 mosaic of the four individual colors after the Log Intensity transformation: (top left) 103a0 (blue); (top right) 103aD (green); (lower left) 103aE (broad band red); (lower right) 103aE (H α). The histograms are one to one with the images above.

UNIVERSITY OF TEXAS AT AUSTIN

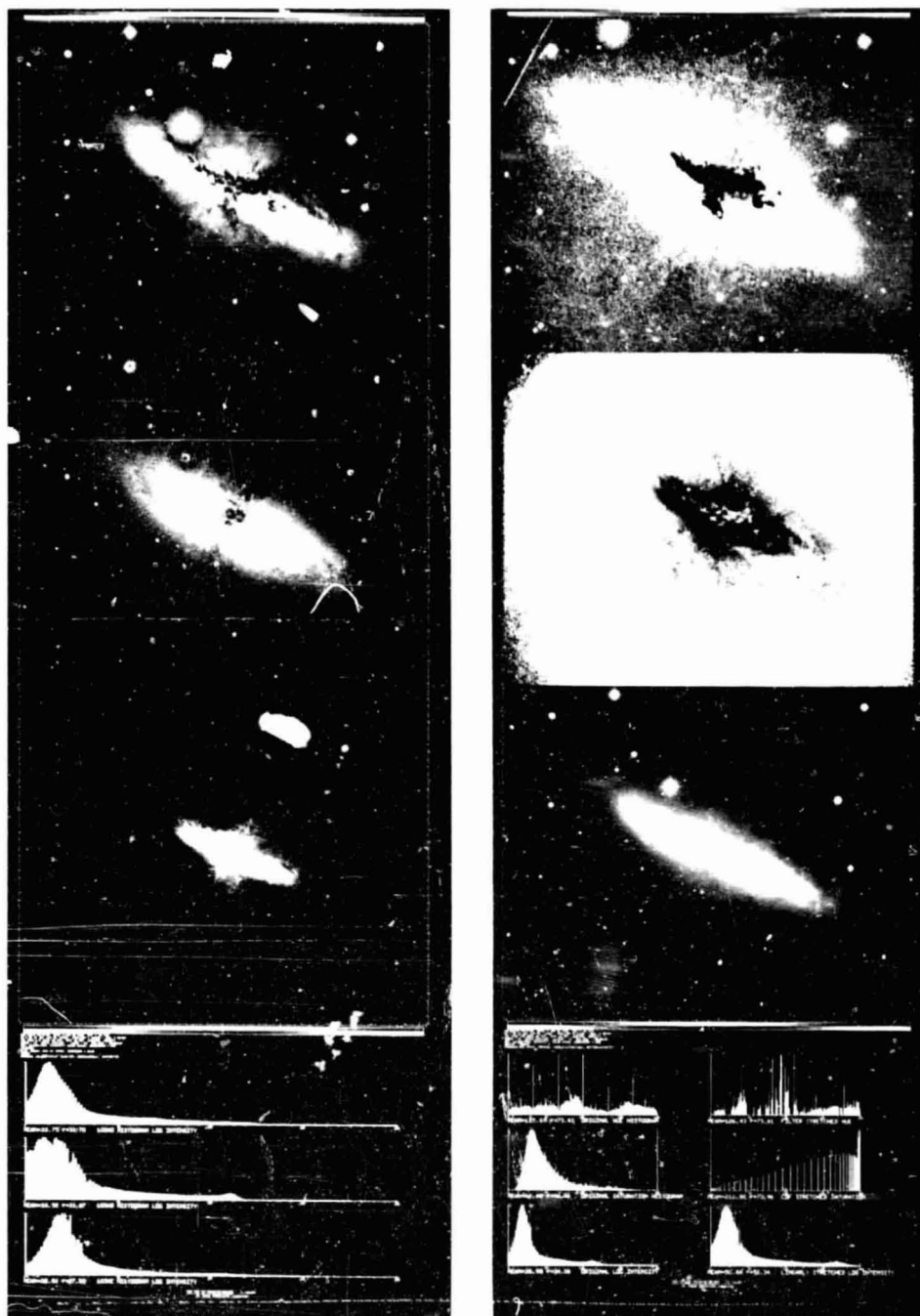


Figure 32. M82 mosaic of three spectral bands. The left column represents images after color enhancement from the hue saturation and intensity transformation. The right column represents top = hue, middle = saturation, bottom = intensity after contrast enhancement of the saturation and filtering of the hue histogram. Histograms beneath the right column of images represent hue, saturation, and intensity in the left column from top down and their enhancements in the right column. From top down, the left column pictures are 103a0, 103aD, and 103aE.

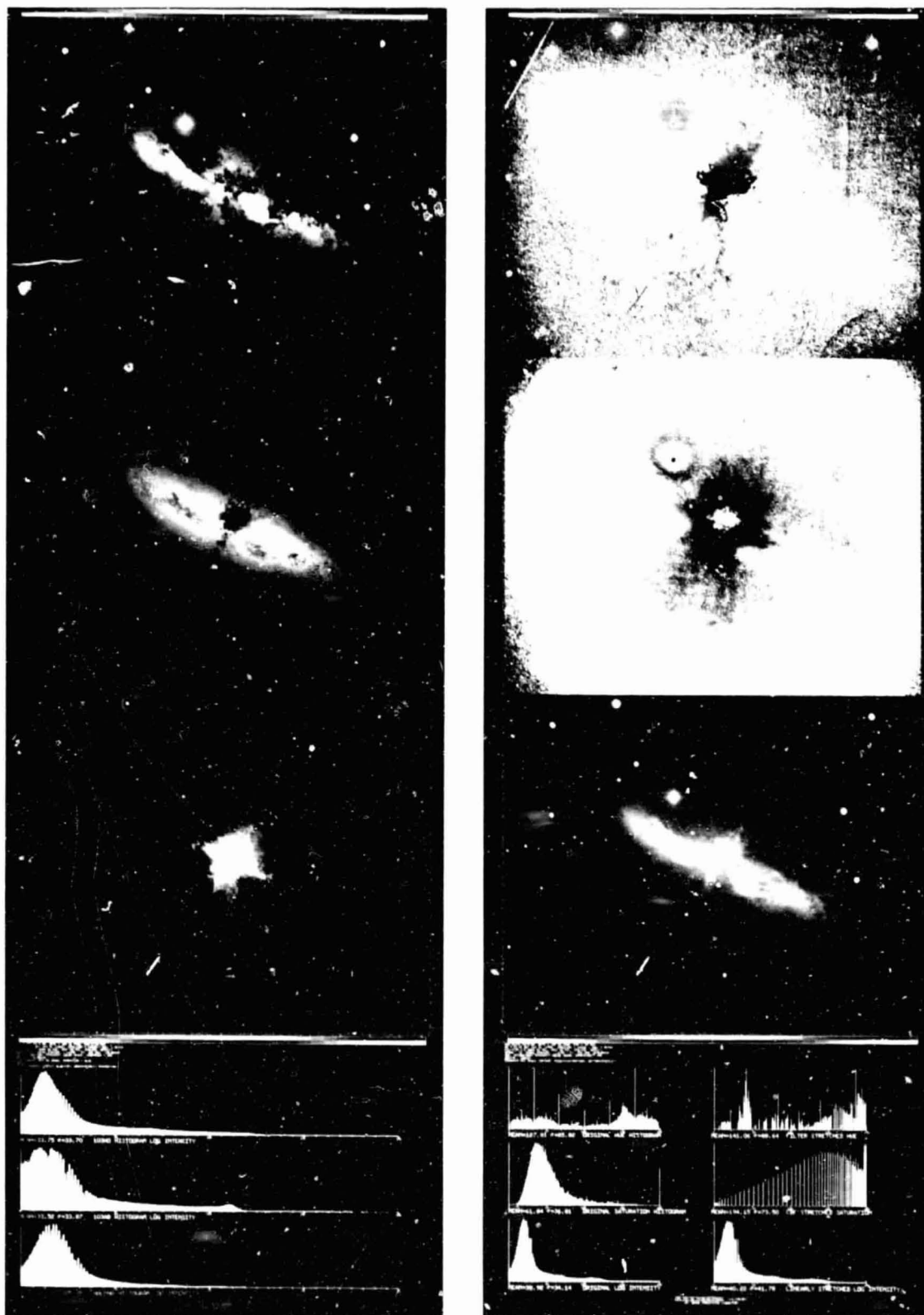


Figure 33. M82 mosaic in the same format as Figure 32. From the top down, the left column pictures are 103a0, 103aD, and H α .

**ORIGINAL PAGE IS
OF POOR QUALITY**

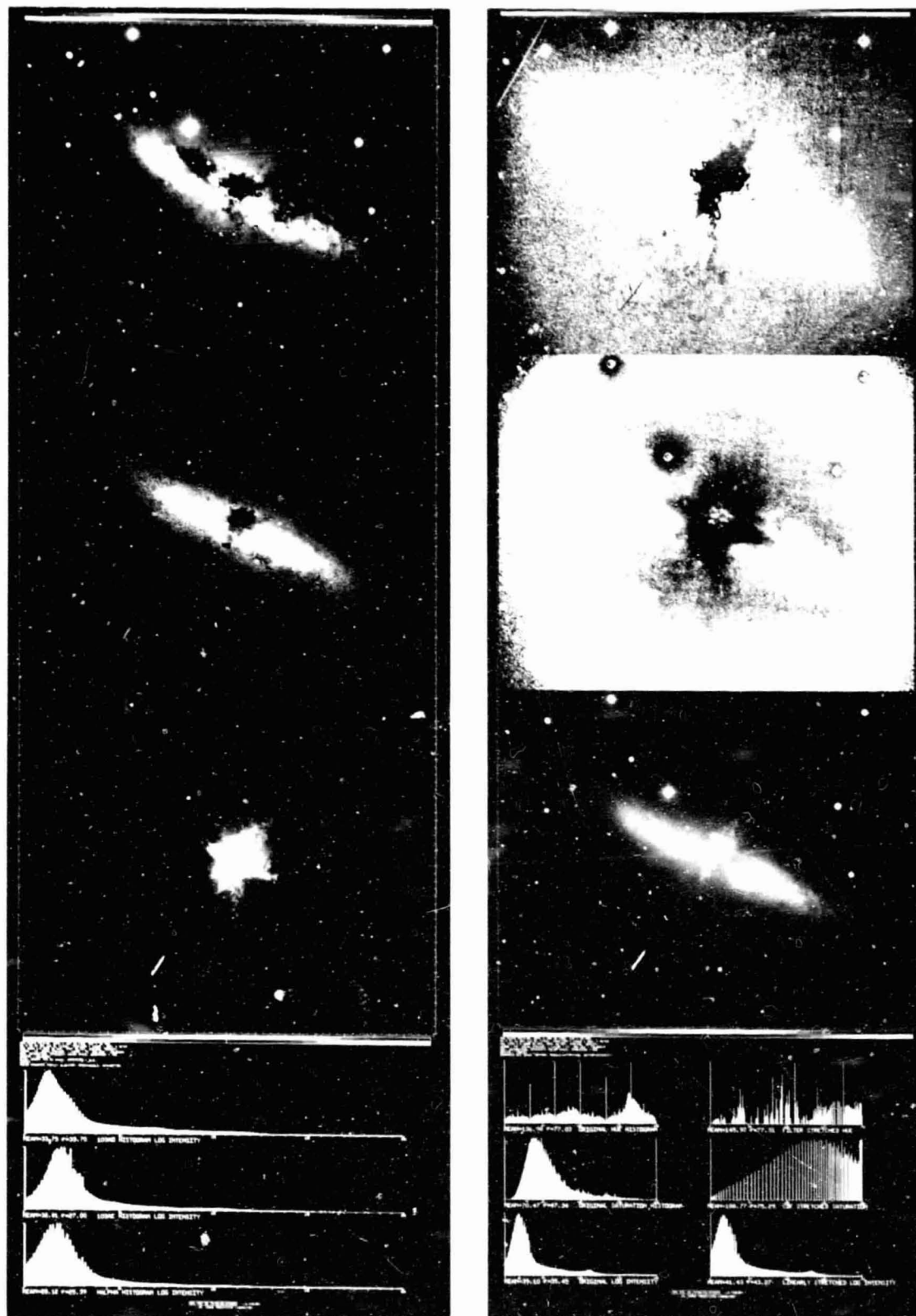


Figure 34. M82 mosaic in the same format as Figure 32. From the top down, the left column pictures are 103a0, 103aE, and H α .

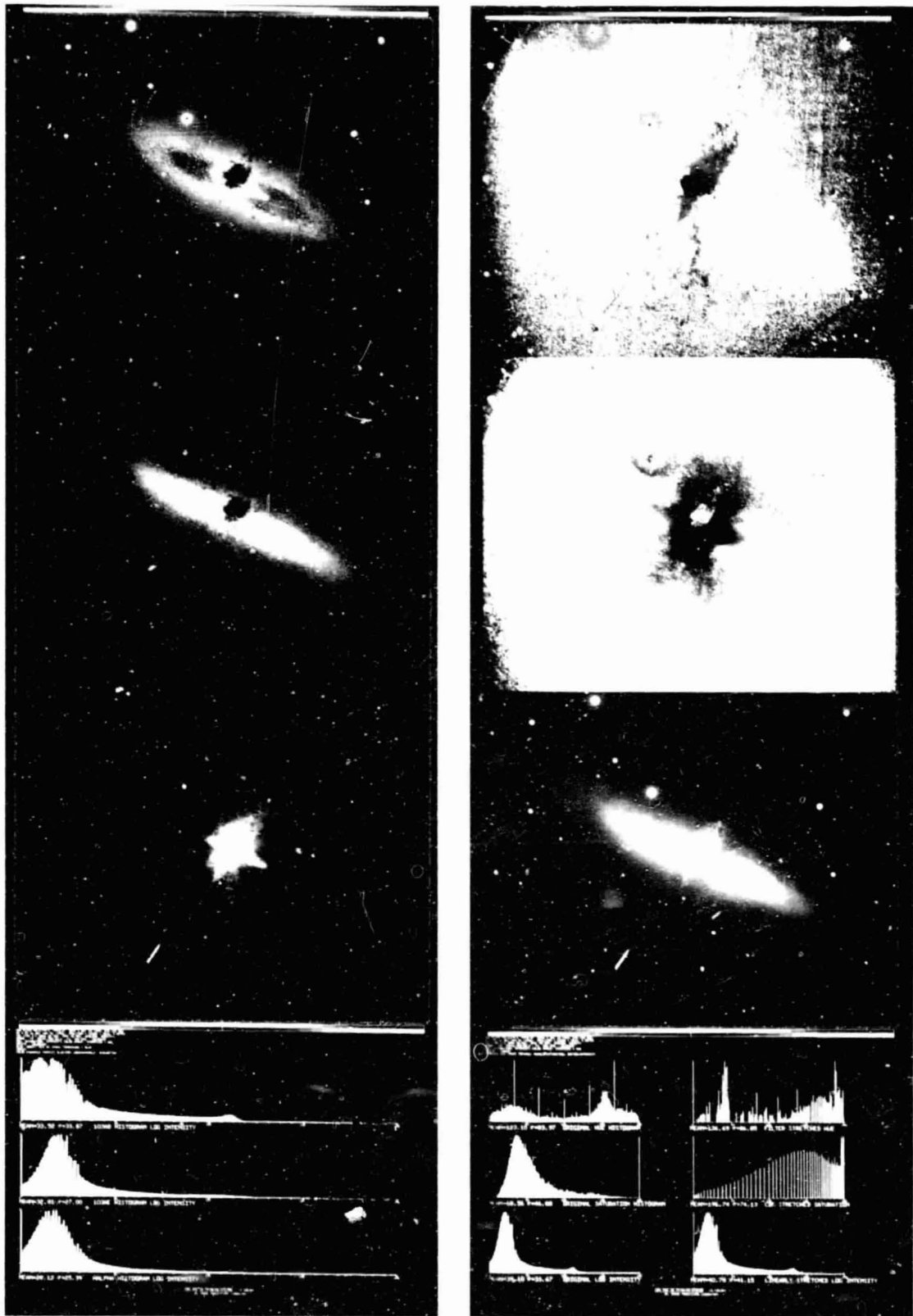


Figure 35. M82 mosaic in the same format as Figure 32. From the top down, the left column pictures are 103aD, 103aE, and H α .

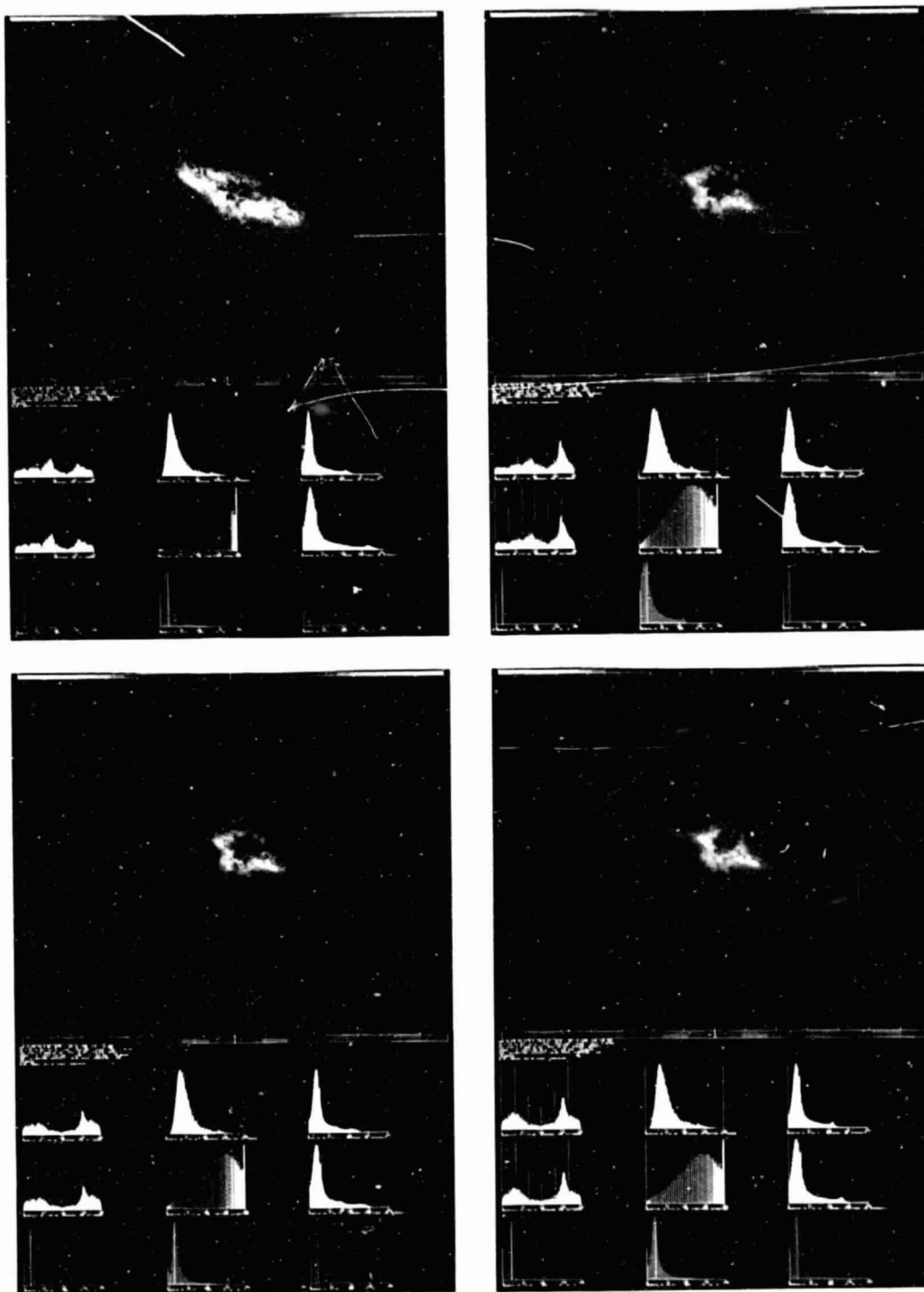


Figure 36. M82 mosaic after HSI color enhancement with the hue, saturation, and intensity transformation and coded with log intensity in equal density steps. See Table 3 for color designations. The histograms below represent from left to right: (top row) hue, saturation, and intensity; (middle row) hue, contrast-enhanced saturation, and contrast-enhanced intensity; (bottom row) blue, green, and red components of the picture. Compare this image with Figure 29.

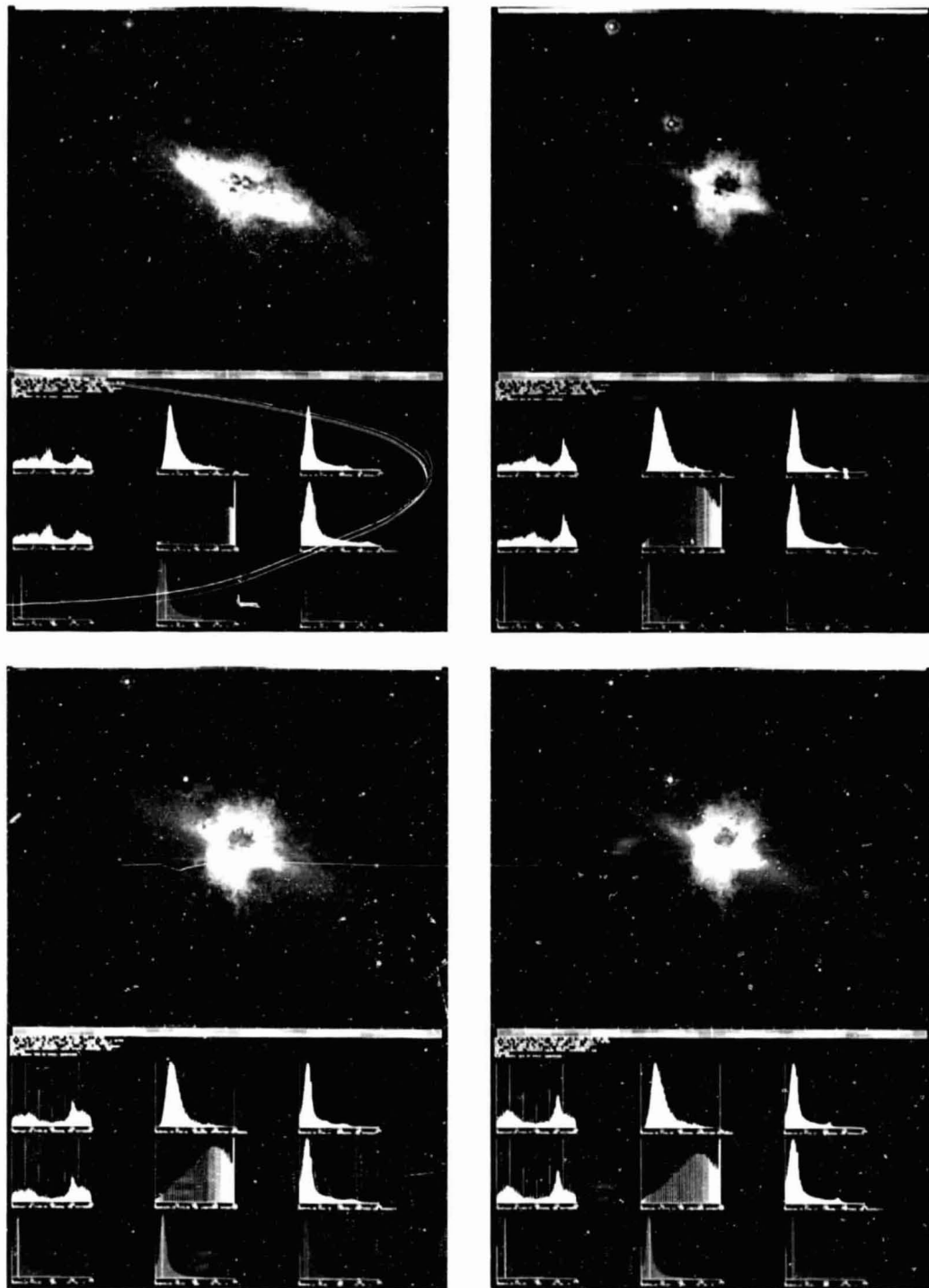


Figure 37. M82 mosaic after HSI color enhancement the same as Figure 36, except with log intensity coded into equal reflectance steps. This version provides better filament detection and truer color consistency over the intensity range. See Table 3 for color designations. Compare this image with Figure 30.

ORIGINAL PAGE IS
OF POOR QUALITY

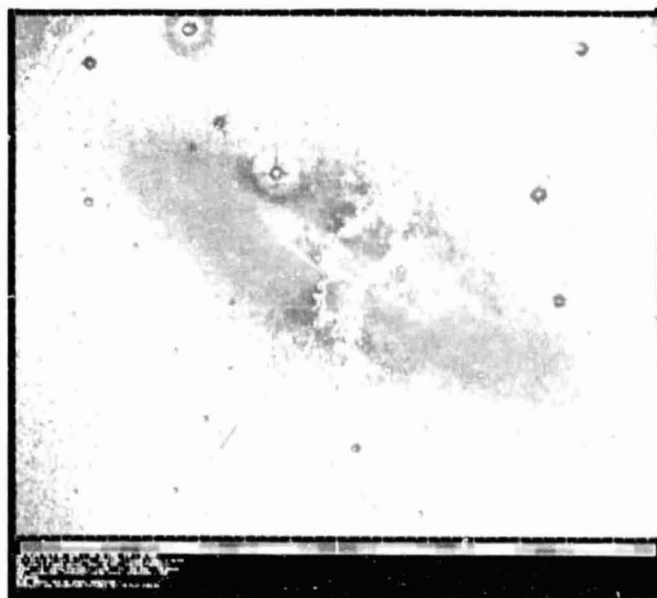


Figure 38. M82 mosaic of pure hue after discarding the saturation and intensity images in the HSI transformation. The color of the sky is dominated by random fluctuations in the emulsion homogeneity. See Table 3 for color designations.

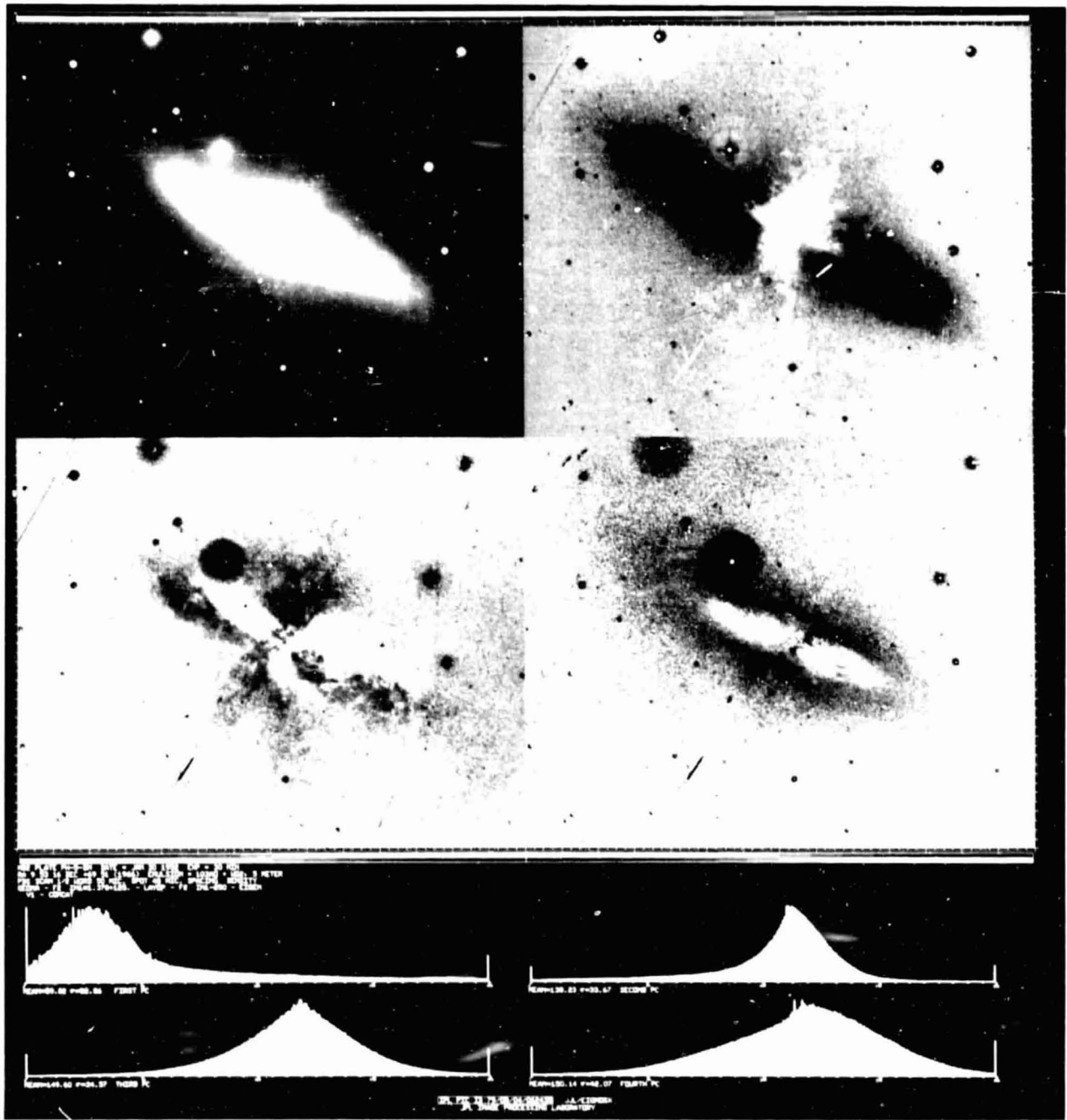


Figure 39. M82 mosaic of the principal component images produced from four spectral bands (Equation 11). The images are ranked in order of descending information content from upper left to lower right in rows as shown in Table 6. Images differ because of color differences and, unlike the original bands, are uncorrelated.

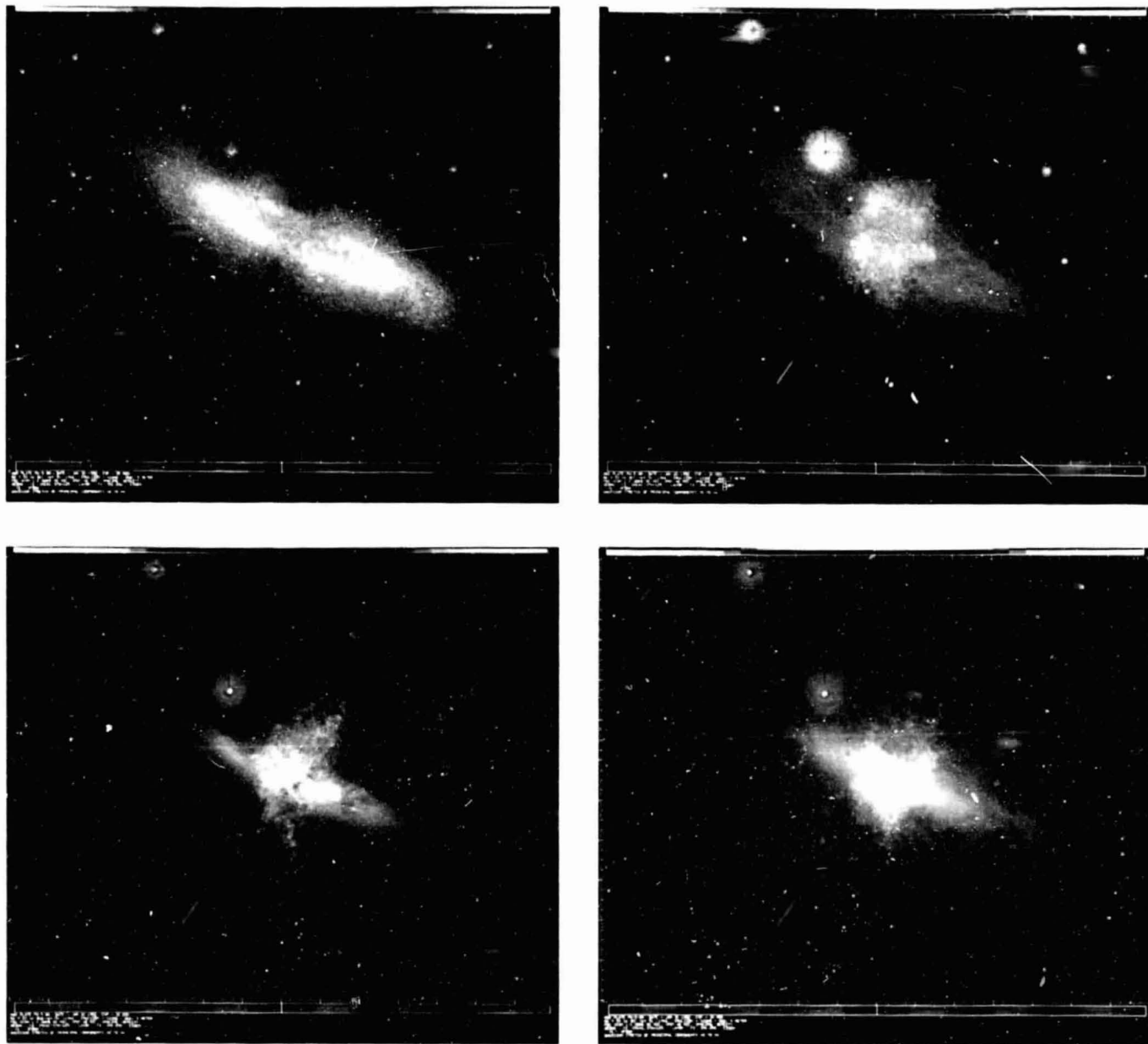


Figure 40. M82 mosaic of color-enhanced reconstructions from the principal component images of Figure 39. See Table 3 for color designations. Compare with Figures 36 and 37.



Figure 41. M82 mosaic of color-enhanced images produced the same way as Figure 40, but with an intermediate filter which smoothed in inverse proportion to the information content of each principal component band.

ORIGINAL PAGE IS
POOR QUALITY

SECTION VII

DECALIBRATION OF CCD ARRAYS

An example of the procedure used to decalibrate a CCD array is included in this section. The array in question was built by Texas Instruments as part of an investigation leading toward the development of the space telescope and Galileo sensors (Reference 13). The array suffers from many defects which will not be present in the final model and should not be considered as a perfected device.

Figure 42 illustrates the raw image of a flat field produced by the CCD. The histograms illustrate the original intensity distribution at left and the contrast-enhanced distribution at right corresponding to the picture above. Several types of artifacts are present. The vertical white lines are due to damaged pixels which continually generate charge while the image is being read out vertically. The black column to the left is due to dead pixels which cannot transfer charge. The short vertical white lines at the top are due to leakage of charge back into the array from the transfer register at the top. The corners of the frame are saturated and are due to large blocks of pixels which continually generate charge (even in the dark current). Overall spatial structure is due to uneven thinning. The only important consideration is whether a pixel responds consistently to an exciting stimulus. If it does, it can be calibrated. Even the linearity of the response is of no importance; vidicons have been routinely calibrated at IPL (References 14 and 15) when their response was nonlinear, spatially dependent, a function of the spatial structure of the scene and of previous scenes.

In the case of the CCD, a first-order correction was applied because of the linearity of the device. No attempt was made to model the leakage to and from the transfer register, leaving this step to another algorithm not addressed here. The calibration consists of generating a large (greater than 15) number of flat field frames at known exposure values. Dark current frames are subtracted from each flat field. For each pixel, a straight line is fit by least squares to all of that pixel's values in all of the frames, relating exposure to response. The coefficients of this line are stored in a dataset for each pixel. Figures 43 and 44 show pictures of the slope and offset coefficients of a typical calibration file. To decalibrate a frame each pixel is reverse transformed using the appropriate coefficients and then scaled to the output.

Figure 45 contains the decalibrated version of Figure 42. The histograms from left to right correspond to the original scene, the decalibrated picture scaled to the same mean value as the original frame, and the contrast-enhanced frame above. The histogram of the decalibrated frame is much narrower, approaching the ideal delta function of the true input stimulus. Only the random noise, integer truncation, and blemish structure in the image, which does not conform to the linear calibration model, give the histogram its final shape. The RMS error obtained from the output histogram agrees to within a few percent of the expected RMS error from theoretical considerations. The dark corners of the

decalibrated image and calibration files are due to inadequate unsaturated data for fitting the linear model.

A display of the stability of each pixel is presented in Figure 46. This picture contains the variance of each pixel as computed from six flat field frames taken at identical exposure times. Large values indicate large uncertainty (poor repeatability). Notice that high variances do not necessarily correspond with blemishes in Figure 42. The large curved contours are due merely to the dynamic range available to the image. Certain pixels will appear less stable if the fractional value to be expressed in integer form lies close to the decision point midway between two integers.

The use of least squares techniques in radiometric calibration can eliminate the noise from calibration files and dark currents alike, leaving the noise in the image as the only noise source. Another advantage of this approach is that it permits the use of higher order functions than linear to be used to model the light transfer function in the event that the device is nonlinear. This frees one from piecewise calibration files.

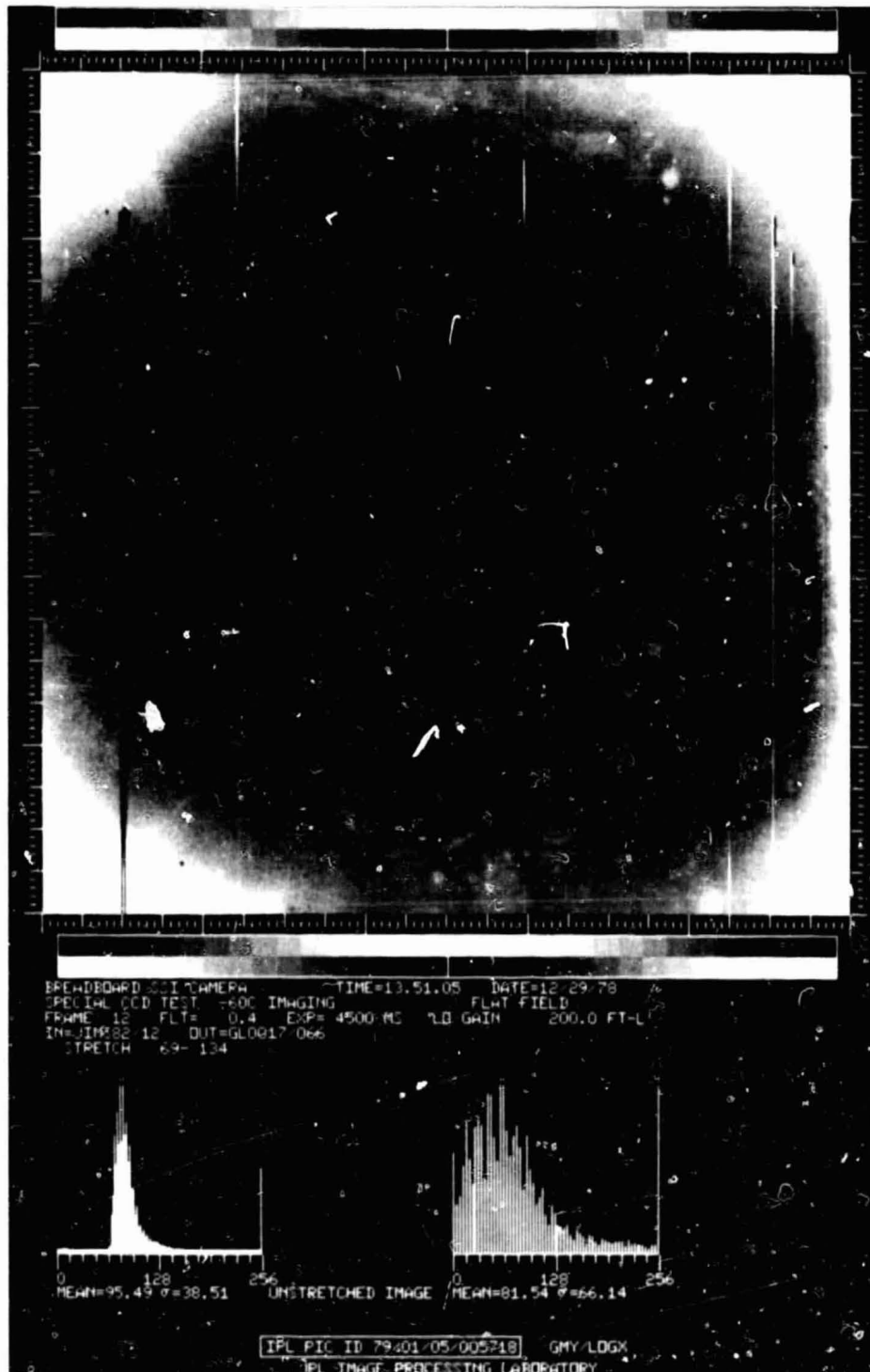


Figure 42. Scaled display of the response of a CCD array to a flat field stimulus. Large scale structure is due to uneven thinning. Vertical blemishes are due to dead pixels, continuously active pixels, and leakage from the transfer register into the picture. The only important consideration is repeatability.

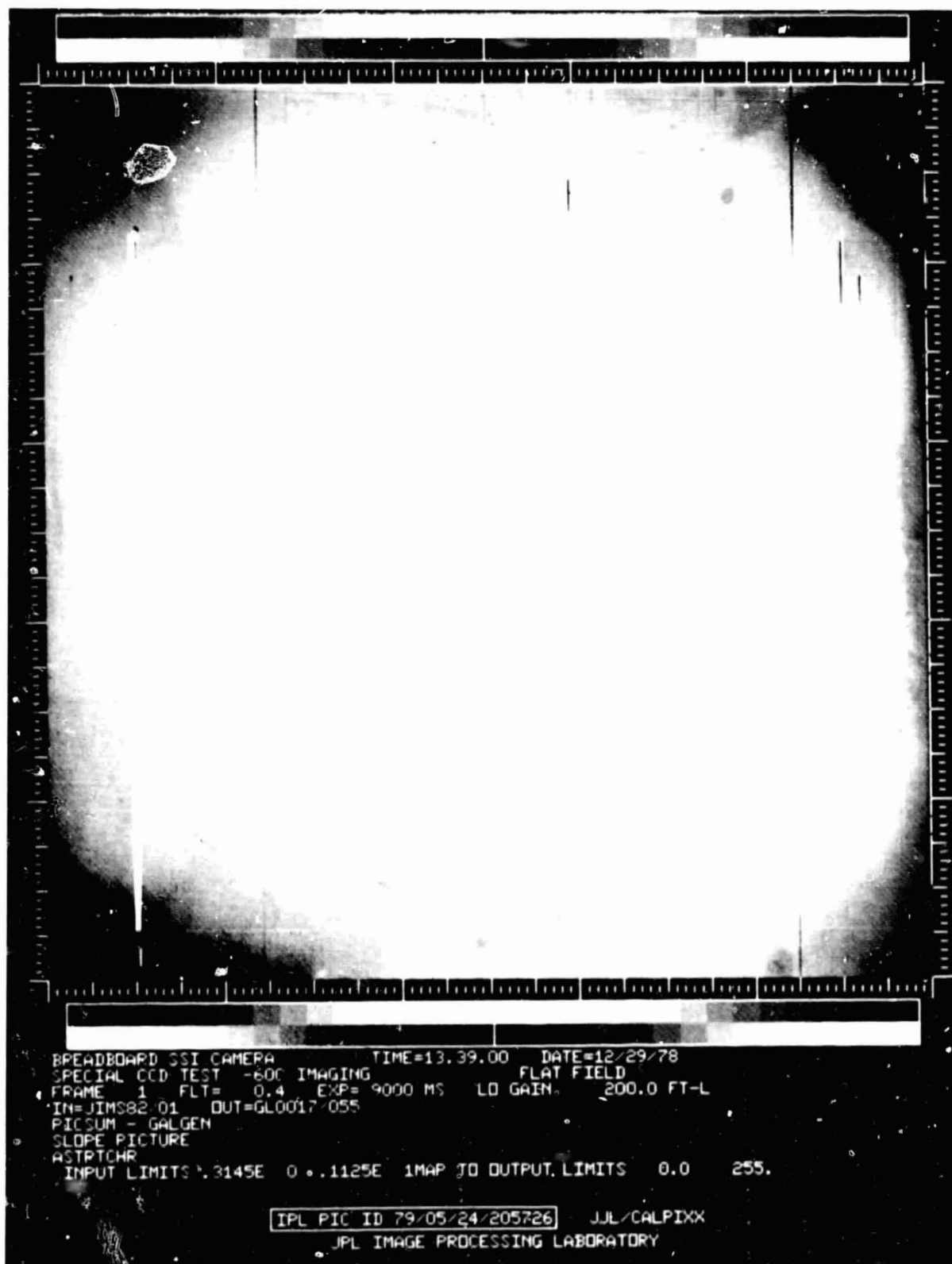


Figure 43. Scaled display of the multiplicative term of the calibration file used to decalibrate the CCD image of Figure 42

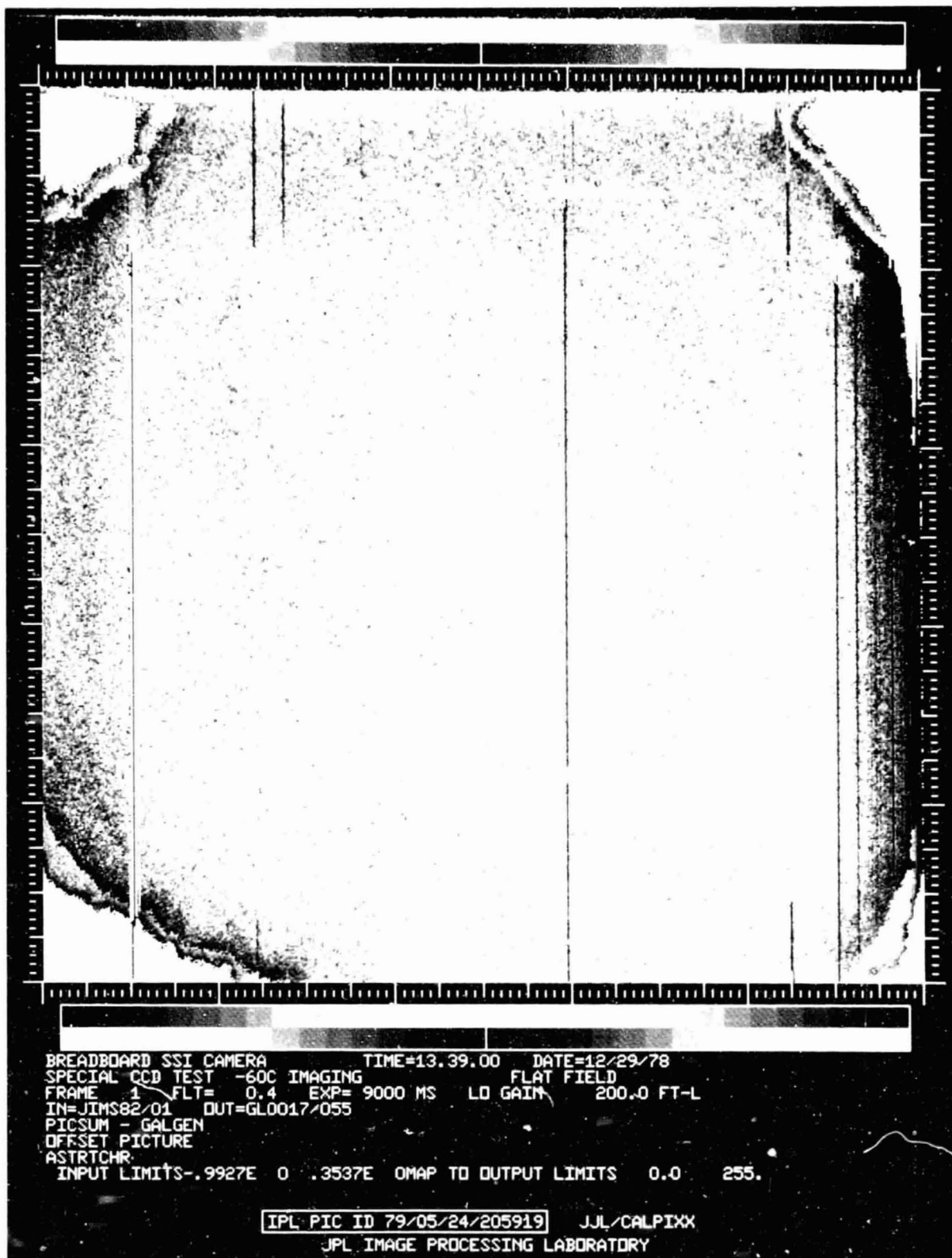


Figure 44. Scaled display of the offset term of the calibration file used to decalibrate the CCD image of Figure 42

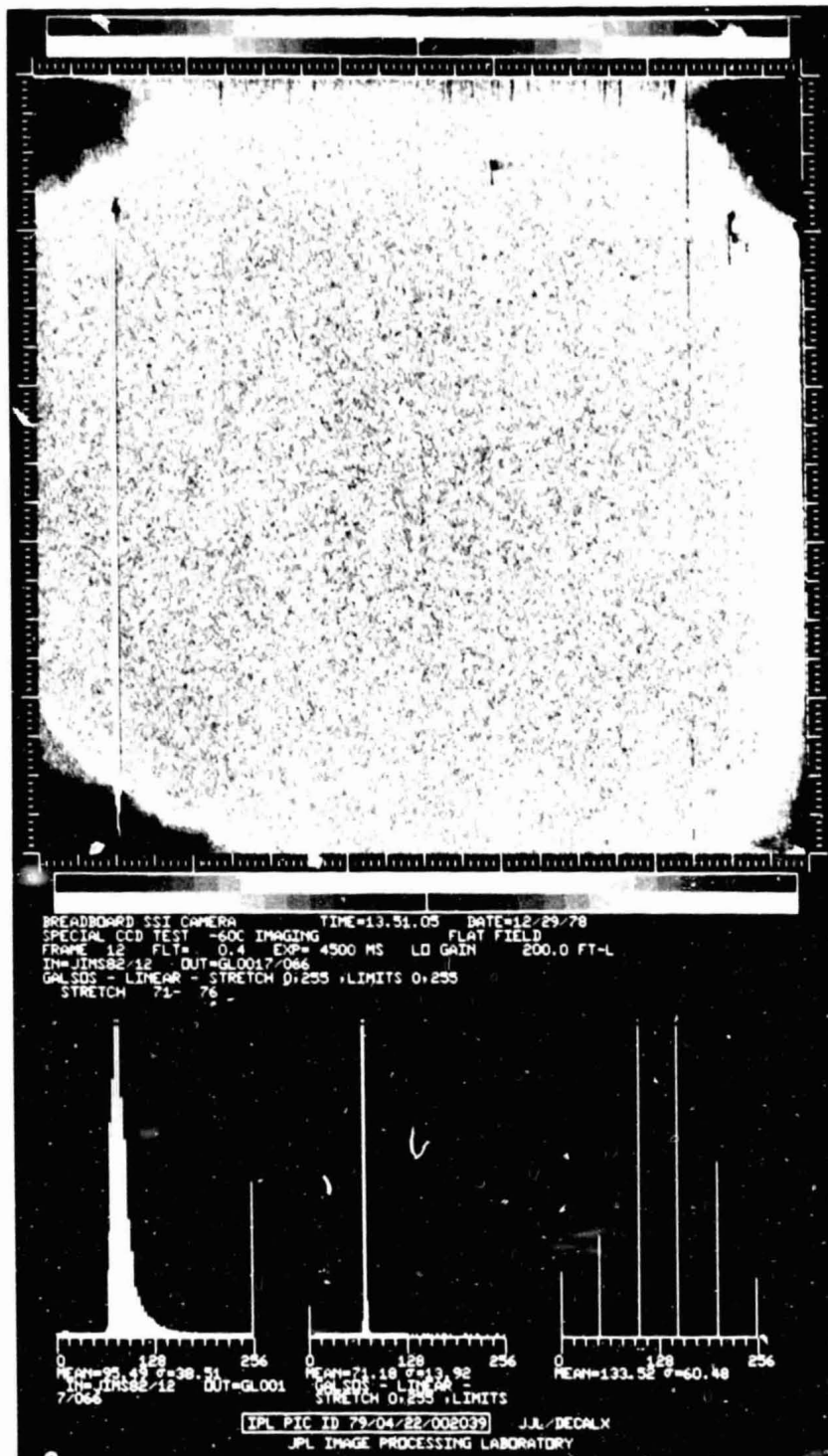


Figure 45. Scaled decalibrated CCD flat field image. The histograms are from left to right (1) from the original flat field image (Figure 42), (2) from the decalibrated image, and (3) from the contrast-enhanced decalibrated image above. Many pixels included in blemishes have also responded to the decalibration operation.

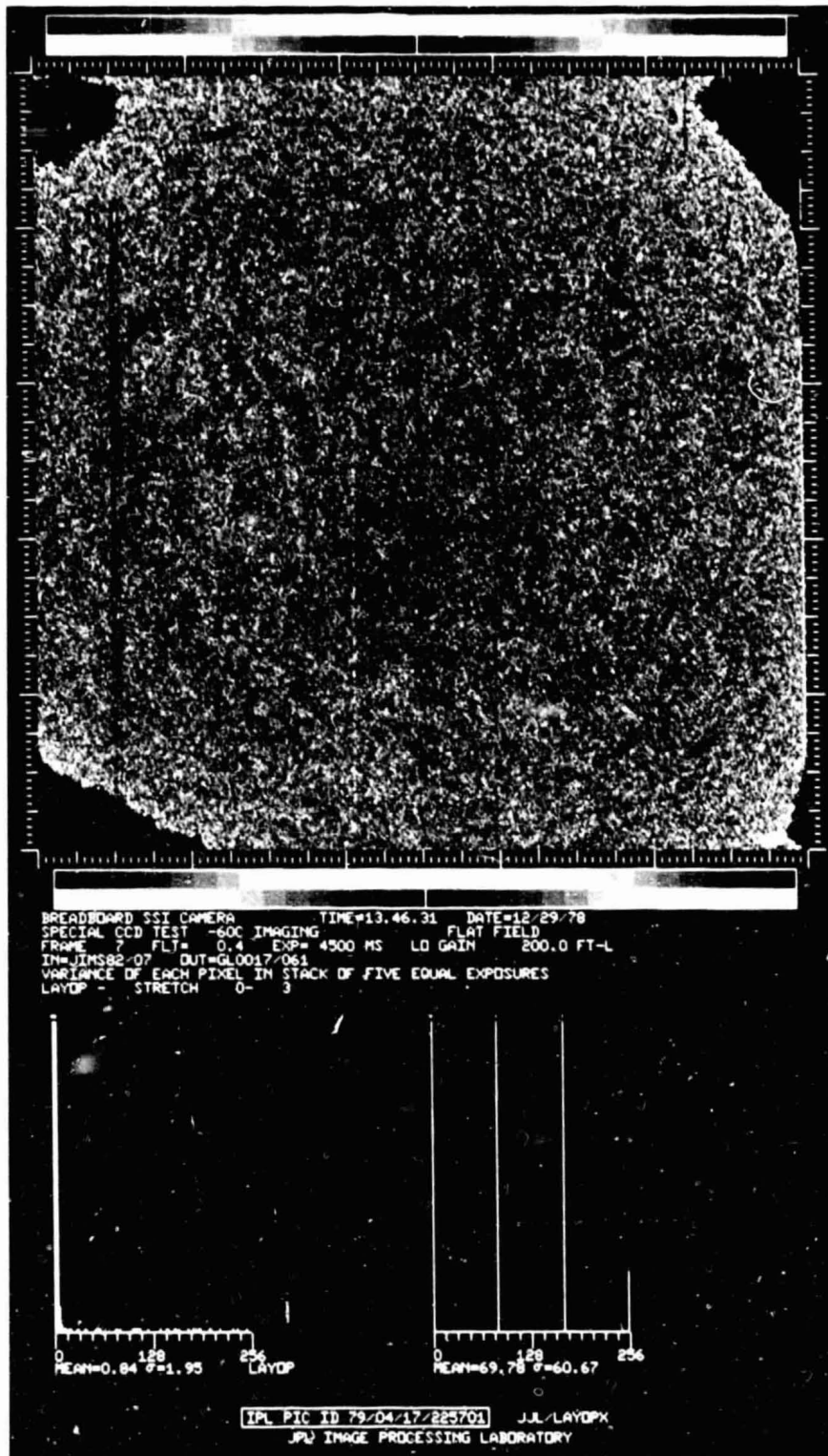


Figure 46. Variance image displaying the variances of each pixel in a set of five identical exposures in an undecalibrated field. Lower histograms represent the variance at left and the scaled variance of the above image at right.

SECTION VIII

SUMMARY AND CONCLUSIONS

From the preceding sections the following conclusions have been reached.

- (1) The Gull maximum entropy technique of restoring convolved imagery is not able to enhance resolution more than linear techniques. It may, however, prove valuable in analysis of objects whose true nature cannot be predicted because it generates images virtually free of artifacts. This is not the case for one-dimensional data.
- (2) Maps of the spatial distribution of polarization in galaxies can be generated from photographic data if the intensity of the images shows differences between intensities or sums of intensities that are greater than the RMS noise bars.
- (3) Temporal changes in objects observed over long-time baselines can be observed by differencing suitably normalized images.
- (4) Maps of the spatial distribution of ionization, temperature, and electron density can be generated for planetary nebulae.
- (5) Investigations of the three-dimensional nature of planetary nebulae are possible by observing the value and sign of the volume emission coefficient using Abel transformations or their equivalent.
- (6) The large dynamic range inherent in galaxies can be reduced into the narrower range available for display devices in such a way that colors in the original scene are not destroyed. A logarithmic intensity compression is advantageous for galaxies.
- (7) The Hue, Saturation, and Intensity transformation and the Principal Component transformation can both be used to enhance subtle color differences without scrambling the hues in the scene. The latter can optimize the visible information content of multispectral images by adjusting the transformation to the statistics of the scene.
- (8) CCD arrays can be modeled by least squares generated flat field calibration files which offer low noise storage, a selection of orders for the function to be used in fitting the light transfer curve, and freedom from piecewise-linear models. These files decalibrate images to theoretical device performance levels.

REFERENCES

1. Lorre, J. J., and Lynn, D. J., Application of Digital Image Processing Techniques to Astronomical Imagery 1977, JPL Publication 78-17, Jet Propulsion Laboratory, Pasadena, Calif., April 15, 1978.
2. Lorre, J. J., Application of Digital Image Processing Techniques to Astronomical Imagery 1978, JPL Publication 78-91, Jet Propulsion Laboratory, Pasadena, Calif., November 1, 1978.
3. Gull, S. F., and Daniell, G. J., "Image Reconstruction From Incomplete and Noisy Data," Nature, Vol. 272, No. 5655, pp. 686-690, April 20, 1978.
4. Frieden, B. R., "Restoring With Maximum Likelihood and Maximum Entropy," J. Opt. Soc. Amer., Vol. 62, pp. 511-518, 1972.
5. Frieden, B. R., and Wells, D. C., "Restoring With Maximum Entropy III. Poisson Sources and Backgrounds," J. Opt. Soc. Amer., Vol. 68, No. 1, pp. 93-103, January 1978.
6. Arp, H., and Lorre, J. J., "Image Processing of Galaxy Photographs," ApJ, Vol. 210, pp. 58-64, November 15, 1976.
7. Lorre, J. J., Lynn, D. J., and Benton, W. D., "Recent Developments at JPL in the Application of Digital Image Processing Techniques to Astronomical Images," SPIE Conference on Image Processing, Asilomar, California, Vol. 74, pp. 234, February 1976.
8. Visvanathan, N., and Sandage, A., "Linear Polarization of the H α Emission Line in the Halo of M82 and the Radiation Mechanism of the Filaments," ApJ, Vol. 176, pp. 57-74, August 15, 1972.
9. Sulentic, J. W., Arp, H., and Lorre, J. J., "Some Properties of the Knots in the M87 Jet," ApJ, in press.
10. Osterbrock, D. E., Astrophysics of Gaseous Nebulae, W. H. Freeman & Co., San Francisco, Calif., 1974.
11. Lorre, J., "Enhancement of the Jets in NGC1097," ApJ, Vol. 222, No. 3, Part 2, pp. L99-L103, June 15, 1978.
12. Madura, D. P., Color Enhancement of Landsat Agricultural Imagery, JPL Publication 78-102, Jet Propulsion Laboratory, Pasadena, Calif., December 15, 1978.
13. Landauer, F. P., et al., "An 800-by-800 CCD Imager for Space-Borne Scientific Imaging," GOMAC 1978 Digest of Technical Papers, November 14-16, 1978.
14. Soha, J. M., "IPL Processing of the Mariner 10 Images of Mercury," JGR, Vol. 80, No. 7, pp. 2394-2414, June 10, 1975.
15. Benesh, M., Voyager Imaging Science Subsystem Calibration Report, JPL Publication 618-802, Jet Propulsion Laboratory, Pasadena, Calif., July 31, 1978.